POLITECNICO DI TORINO
Repository ISTITUZIONALE

High Damping Rubber Bearings: Optimal models evaluation considering production variability

Original
High Damping Rubber Bearings: Optimal models evaluation considering production variability / Cucuzza, R., LONDONO LOPEZ, S., Domaneschi, M., Greco, R., Marano, G.C.. - In: STRUCTURES. - ISSN 2352-0124. - 73:(2025), pp. 1-19. [10.1016/j.istruc.2025.108355]

Availability:
This version is available at: 11583/2997583 since: 2025-02-18T15:30:06Z

Publisher:
Elsevier

Published
DOI:10.1016/j.istruc.2025.108355

Terms of use:

This article is made available under terms and conditions as specified in the corresponding bibliographic description in the repository

Publisher copyright

(Article begins on next page)

25 November 2026

Structures 73 (2025) 108355



Contents lists available at ScienceDirect

Structures

journal homepage: www.elsevier.com/locate/structures





High Damping Rubber Bearings: Optimal models evaluation considering production variability

Raffaele Cucuzza [a,b], Santiago Londoño [b], Marco Domaneschi [b,c,*], Rita Greco [d], Giuseppe Carlo Marano [b]

[a] College of Civil Engineering, Henan University of Technology, Zhengzhou, Henan Province, China
[b] Dipartimento di Ingegneria Strutturale, Edile e Geotecnica (DISEG), Politecnico di Torino, Corso Duca Degli Abruzzi, 24, Turin, 10128, Italy
[c] International Institute for Urban Systems Engineering, Southeast University, 2 Sipailou, Nanjing, 210096, China[1]
[d] Dipartimento di Ingegneria Civile, Ambientale, del Territorio, Edile e di Chimica, Politecnico di Bari, via Edoardo Orabona, 4, Bari, 70126, Italy

ARTICLE INFO

Keywords:
High Damping Rubber Bearings
Numerical modeling
Optimization
Genetic algorithm
Seismic device
Manufacturing variability

ABSTRACT

Seismic isolation has become an effective technique for seismic protection, significantly reducing lateral forces and horizontal accelerations in buildings. Among various isolation devices, High Damping Rubber Bearings are widely used due to their cost-effectiveness, ease of application, and clear mechanical behavior during the design phase. A precise mechanical behavior model is essential for the efficient use of High Damping Rubber Bearings in practice, as it realistically mitigates seismic actions on protected structures. The design of these systems mandates a permissible displacement limit under seismic conditions, beyond which the mechanical performance and operational functionality of the bearings may be compromised. This paper focuses on the optimal selection of mechanical behavior models for High Damping Rubber Bearings, constrained by the maximum design displacement to prevent phenomena such as pinching. The primary innovation lies in evaluating not only the accuracy but also the stability of mechanical parameters derived from standard experimental tests, as specified by construction guidelines. The research investigates the mechanical behavior within the limits of maximum design displacement, ensuring alignment with practical design scenarios and addressing relevant mechanical responses under typical service conditions. Moreover, it provides a reliable assessment approach for the assessment of the real industrial production variability of such devices, emphasizing the effect of uncertainties induced in manufacturing, and the need for robust, adaptable design models to accommodate such variability. Six established High Damping Rubber Bearings models were evaluated through experimental tests on ten samples. The analysis revealed that models with higher accuracy in reproducing the experimental behavior of a specific device might fail to represent the variability found in industrial production. This highlights the importance of balancing accuracy and robustness in the model's selection for practical applications.

1. Introduction

Civil engineers have long been concerned with the interactions between designed structures and environmental forces, particularly the impact of earthquakes. Among various mitigation strategies, isolation has played a major role for this purpose [1]. Nakashima [2] has highlighted the advantages of isolated structures and advocated for the use of Building Isolation Systems (BIS) [3], particularly during strong seismic events such as the one experienced in Kobe in '95 or the one in Northridge in '94.

BIS is a technique that shifts a structure's fundamental natural period to a longer period range by installing special devices at its base, effectively decoupling the structure from ground motion. During an earthquake, this approach reduces floor acceleration and inter-story drift compared to a non-isolated structure, thereby allowing it to remain elastic or nearly elastic [4]. Interest in BIS has grown over time, resulting in several established technical solutions [5], and new developments in innovative research in the field (e.g., [6,7]). The evolution of BIS is based on lessons learned from major seismic events and the need to enhance protection measures against such

* Corresponding author at: Dipartimento di Ingegneria Strutturale, Edile e Geotecnica (DISEG), Politecnico di Torino, Corso Duca Degli Abruzzi, 24, Turin, 10128, Italy.
E-mail address: marco.domaneschi@polito.it (M. Domaneschi).
[1] Visiting Professor.

https://doi.org/10.1016/j.istruc.2025.108355
Received 20 November 2024; Received in revised form 15 January 2025; Accepted 31 January 2025
Available online 18 February 2025
2352-0124/© 2025 The Authors. Published by Elsevier Ltd on behalf of Institution of Structural Engineers. This is an open access article under the CC BY-NC-ND license (http://creativecommons.org/licenses/by-nc-nd/4.0/).

catastrophic occurrences [8,9]. According to the Architectural Institute of Japan [10], BIS design has adapted along its historical classification periods, mainly in the improvement of three key device characteristics: design vibration period (T_{ISO}) increasing from 2 s to 10 s, design displacement (δ) enlarging the gap from 10–20 cm to 40 cm, and device diameter (ϕ) passing from 400–600 mm to 1300 mm.

Among the isolation devices, High Damping Rubber Bearings (HDRB) emerged as a cost-effective solution to protect the structures during a seismic event [11]. These bearings consist of a rubber compound that exhibits high damping properties, meaning it absorbs and dissipates energy effectively during a ground motion [12]. The rubber body allows to withstand horizontal displacements while providing vertical load-bearing capacity, both properties derive into the reduction of the seismic forces transmitted to the structure and enhance its resilience against earthquake damage [13,14].

The success of HDRBs lies in their simplicity, relative cost-effectiveness, ease of installation, and the ability to accurately model their behavior under design actions. HDRBs exhibit a primarily non linear softening behavior, coupled with progressive energy dissipation, as long as the maximum displacement does not exceed approximately 100% of the bearing's rubber thickness [15]. This behavior effectively decouples the response of the superstructure from the foundation, shifting into a spectral zone where seismic forces are significantly reduced. It is essential in design practice to ensure that the maximum displacement under the design earthquake does not exceed the limited value [16], beyond which the mechanical behavior may change, leading to progressive stiffness recovery (pinching) and potential damage to the bearings. Such damage could include delamination, excessive rubber deformation, or slippage at the steel plate interfaces.

HDRBs offer a number of advantages over other seismic isolation devices and mitigation techniques. In essence, HDRBs provide simultaneous energy dissipation and deformation capacity within a single device across a broad range of frequencies. Furthermore, HDRBs have well-documented numerical performance and significant durability [17,18]. Their ability to withstand multiple events, and relatively straightforward installation and replacement, further contribute to their positive attributes [19]

The behavior of HDRBs has been extensively studied through the phenomenological modeling of rubber and its intrinsic hysteretic properties for energy dissipation. A review of the literature reveals that a number of factors must be considered, including degradation, pinching, stiffness evolution, hardening, damping, temperature effects, and cyclic stability [20–24].

Capuano et al. [25] classify numerical models into four primary categories based on the equations used to compute output variables. The most computationally efficient are algebraic models, extensively used in literature, design codes, and structural software [26]. First introduced in the mid-20th century, notable examples include the Ramberg–Osgood model [27] and the Giuffrè–Menegotto–Pinto model [28]. These models initially described elastoplastic generalized displacement but did not generate complete hysteresis loops, necessitating the use of the Masing Rule [29,30] as a mathematical complement. Subsequent advancements introduced improved formulations such as the BiLinear Law [31] and the Jankowski model [32], which use a proportional, linear relationship between displacement and force. Despite their simplicity, these models often struggle to replicate hysteretic behavior, including degradation and stiffness variation. To address these limitations, transcendental models were developed. Kikuchi and Aiken [33] introduced a model using trigonometric functions to depict the response of elastomeric bearings, marking a milestone that paved the way for developing more advanced transcendental models. Differential models also emerged to better capture non-linear cyclic behavior by incorporating derivatives, for instance, Ozdemir's widely adopted model [34] that was further explored in subsequent formulations [35]. Finally, models utilizing integral equations are present in the literature. These models effectively quantify stiffness degradation by tracking hysteresis evolution perceived during the integration, though they are less commonly implemented compared to the previously mentioned models.

The growing inclusion of BIS, particularly HDRB, in civil structures and infrastructure, is driving manufacturers to produce these devices in larger quantities, ensuring compliance with the available regulations and latest scientific developments. As a result, the interest in HDRBs' numerical models is rapidly increasing [36].

Despite a well-established literature on this field, the analysis of robustness and accuracy for such models remains an under-explored area. In particular, considering the reliability of their numerical outputs along a production series, it deserves further investigation. To fulfill this gap, a reliability assessment through statistical analysis, ensuring a fine-tuning calibration procedure of the numerical models' parameters based on the experimental data, is herein proposed as a promising approach. This paper analyzes both the accuracy and, more importantly, the stability of mechanical parameters for the reproduction of the experimental horizontal behavior of HDRBs within the requested design limits. Underscoring the research outcomes, the designer will be guided in the identification of the best numerical model able to ensure acceptable levels of accuracy and reliability of the building seismic response by controlling uncertainties deriving from the series production process of HDRBs.

The paper is organized as follows: *Section* 2 presents the numerical models involved in the optimization problem, providing a brief overview of each one. In *Section* 3, the HDRBs description and the laboratory equipment used for dynamic testing are presented. *Section* 4 focuses on the mathematical formulation of the problem and describes the optimization algorithm. *Section* 5 describes the results of the optimization process, showcasing the optimal hysteresis cycles for each model examined. In *Section* 6, the authors conduct a statistical analysis to identify underlying trends and patterns. The findings from the analysis are summarized in *Section* 7, which introduces indices to evaluate the accuracy and robustness of each model. The final discussion, including future directions, is covered in *Section* 8.

2. Numerical models for High Damping Rubber Bearings

Several numerical models formulated to accurately represent the behavior of HDRBs in a range of maximum lateral displacement of almost 100% of the rubber high of the devices (the standard limits in practical design codes worldwide) are available in the literature. The classification of such models depends on the type of equation that must be solved to evaluate the output variable. For the purposes of this research, algebraic, transcendental, and differential models have been distinguished [37]. The parameters of these models can be adjusted by defining an objective function (or cost function) [38,39] to be minimized by an identification process performed through the well-known Genetic Algorithm (GA). The aim is to achieve a satisfactory level of accuracy between the experimental data and the calculated output variable of each model [40–42].

The current section presents a detailed description of the mathematical formulation of most adopted algebraic models, progresses to more complex transcendental models, and then moves on to generalized differential models.

2.1. Bi-linear Model - Law #1 [43]

This traditional model efficiently represents the strain rate-dependent mechanical law, splitting the response into two branches according to the deformation state of the specimen. By introducing the elastic stiffness K_1, the post-elastic stiffness, K_2, and the yielding deformation x_y, the model mimics the conventional elastomeric behavior of isolators recreating a linear-elastic shape [44]. Eq. (1) introduces the

formulation for the previously described behavior.

$$F(x, x_y) = \begin{cases} K_1 \cdot x, & \text{if } x < x_y, \\ K_1 \cdot x_y + K_2 \cdot (x - x_y), & \text{if } x > x_y. \end{cases} \tag{1}$$

Despite the low computational cost, in most cases, this model fall short of representing the actual mechanical behavior of the devices since the expected response is mainly within the non-linear range and characterized by a complex behavior. For this reason, more numerically powerful models are presented in the following sections.

2.2. Jankowski et al. Model - Law #2 [45]

For HDRB devices, the rubber properties are primarily responsible for a highly non-linear hysteretic behavior. This aspect is largely investigated by Jankowski et al. in [46] where a non-linear strain rate-dependent model designed for HDRB devices subjected to a constant vertical load and invariant temperature is assumed. It simulates the horizontal behavior of the device taking into account a nonlinear elastic spring dashpot element.

The mathematical formulation of the adopted numerical model is shown in Eqs. (2)–(3):

$$F = F_1(x(t); \dot{x}(t)) + F_2(x(t); \dot{x}(t)) \tag{2}$$

$$F = K(x(t); \dot{x}(t)) \cdot x(t) + C(x(t); \dot{x}(t)) \cdot (\dot{x}(t)\dot{x}(t)) \tag{3}$$

In these formulas, the shear stiffness, K, and the damping coefficients, C, evaluated at a given time t, are calculated considering the proper values of the experimental deformation $x(t)$ and velocity $\dot{x}(t)$ as reported in the Eqs. (4)–(5).

$$K(x(t), \dot{x}(t)) = a_1 + a_2 x^2(t) + a_3 x^4(t) + \frac{a_4}{\cosh^2\left(a_5 \dot{x}(t)\right)} + \frac{a_6}{\cosh\left(a_7 \dot{x}(t)\right) \cosh\left(a_8 x(t)\right)} \tag{4}$$

$$C(x(t), \dot{x}(t)) = \frac{a_9 + a_{10} x^2(t)}{\sqrt{a_{11}^2 + \dot{x}^2(t)}} \tag{5}$$

In the model, the parameters a_i, for $i = 1, 2..., 11$, are numerically determined by fitting the experimental data using the GA search. In this model, a_1 sets the baseline stiffness level, which is adjusted by a_2 and a_3 for larger shear strains. Parameters a_4 and a_5 regulate stiffness near maximum displacements, while a_6 to a_8 increase stiffness for lower amplitude movements. Finally, parameters a_9 to a_{11} modify the degree of damping to shape the loops as desired [46].

2.3. Vaiana et al. Model - Law #3 [47]

Aiming to improve the accuracy and the computationally efficient of the numerical models, Vaina et al. suggested an extension of the uniaxial symmetric rate-independent model presented by Kikuchi and Aiken [48], Vaina's Complex Asymmetric mechanical hysteresis model introduces the evaluation of the generalized force by solving a scalar equation and employing only one history-dependent variable [49].

The model aims to resolve two specific instances of the system: first, targeting the asymmetric bilinear trend, and second, the exponential trend. Practically, it allows the reproduce a wide range of asymmetric hysteretic formulations. To compute the model generalized force, four curves are calculated aiming to characterize the shape of a standard asymmetric hysteresis loop [50].

Eq. (6) calculates the generalized horizontal isolator's response force, utilizing a decision-making scheme based on the deformation level at each time step relative to a control value determined by Eqs. (11)–(12).

Eq. (8) expresses the first two curves where C_u and C_l represent the upper and lower limit of the graph, respectively. For the second component C^+ and C^- instead represent the loading and unloading trends (see Eq. (7)).

$$f\left(u, u_j^+\right) = \begin{cases} c^+\left(u, u_j^+\right) & u < u_j^+ \\ c_u(u) & u > u_j^+ \end{cases} \tag{6}$$

$$f\left(u, u_j^-\right) = \begin{cases} c^-\left(u, u_j^-\right) & u > u_j^- \\ c_l(u) & u < u_j^- \end{cases}$$

$$c^+\left(u, u_j^+\right) = f_e^+(u) + K_b{}^+ u + f_0^+ - \frac{1}{\alpha^+}\left[e^{-\alpha^+\left(+u - u_j^+ + \bar{u}^+\right)} - e^{-\alpha^+ \bar{u}^+}\right] \tag{7}$$

$$c^-\left(u, u_j^-\right) = f_e^-(u) + K_b{}^- u - f_0^- + \frac{1}{\alpha^-}\left[e^{-\alpha^-\left(-u + u_j + + \bar{u}^-\right)} - e^{-\alpha^- \bar{u}^-}\right]$$

$$c_u(u) = f_e^+(u) + K_b{}^+ u + f_0^+ \tag{8}$$

$$c_l(u) = f_e^-(u) + K_b{}^- u - f_0^-$$

$$f_e^+(u) = \beta_1^+ e^{\beta_2^+ u} - \beta_1^+ + \frac{4\gamma_1^+}{1 + e^{-\gamma_2 + (u - \gamma_3 +)}} - 2\gamma_1^+ \tag{9}$$

$$f_e^-(u) = \beta_1^- e^{\beta_2^- u} - \beta_1^- + \frac{4\gamma_1^-}{1 + e^{-\gamma_2^-\left(u - \gamma_3^-\right)}} - 2\gamma_1^- \tag{10}$$

$$u_j^+ = u_P + \bar{u}^+ + \frac{1}{\alpha^+} \ln\left\{+\alpha^+\left[f_e^+\left(u_P\right) + K_b{}^+ u_P + f_0^+ + \frac{1}{\alpha^+} e^{-\alpha^+ \bar{u}^+} - f_P\right]\right\} \tag{11}$$

$$u_j^- = u_P - \bar{u}^- - \frac{1}{\alpha^-} \ln\left\{-\alpha^-\left[f_e^-\left(u_P\right) + K_b{}^- u_P - f_0^- - \frac{1}{\alpha^-} e^{-\alpha^- \bar{u}^-} - f_P\right]\right\} \tag{12}$$

The Eqs. (7) to (12) are calculated considering 16 parameters to control the shape of the output force cycles, the pre-yielding and post-yielding initial stiffness components are influenced by K_b, F_o and α when the device experiences the maximum cyclic displacement while stiffness and shape are controlled by the parameters β_1 and β_2 by varying the degree of damping. Specifically, the parameters γ_1, γ_2 and γ_3, are introduced in the equation to account for pinching and post-hardening effects. However, as discussed in the next Sections 4.1 and 5, these parameters are set to zero since their contribution to reproduce the experimental input is negligible. This adjustment is made because the experimental data exclusively covers serviceability testing, where degradation and secondary effects are not observed.

2.4. Bouc Wen Model - Law #4 [51]

Bouc Wen's hysteresis model can be considered as one of the most successful differential models and it is widely used by practitioners for its simplicity in modeling and well-known performance in reproducing the experimental output. The choice of this formulation to represent the force output of the HDRB is supported by the model's robustness in both mathematics and physics, as well as the agreement between experimental and numerical data that has emerged in the literature review [52].

The mathematical formulation of such a model is reported in Eq. (13):

$$F(t) = \alpha K_i x(t) + (1 - \alpha) K_i z(t) \tag{13}$$

In this context, $x(t)$ represents the experimental deformation, $z(t)$ is the variable that characterizes the hysteretic response, while K_i represents the model's stiffness before yielding. Additionally, α denotes the ratio of stiffness before and after yielding [52,53].

$$\frac{dz}{dt} = A \cdot \frac{dx}{dt} - \left(\beta \cdot \left|\frac{dx}{dt}\right| \cdot z \cdot |z|^{\eta - 1}\right) - \left(\gamma \cdot \frac{dx}{dt} \cdot |z|^{\eta}\right) \tag{14}$$

The hysteretic variable $z(t)$ is introduced by defining the differential component of the model as observed in Eq. (14).

The parameters A, β, γ, and n are time-invariant constants that control the shape and amplitude of the hysteresis cycle, the linearity of the unloading branch, and the smoothness of the transition between pre-yielding and post-yielding phases, respectively. More in detail, A relates to the initial stiffness, β affects the amplitude of the hysteresis cycle and the level of energy dissipation, γ manages the linearity of the unloading curve, and n smooths the transition between different yielding phases.

2.5. Abe et al. Model - Law #5 [54]

Abe et al. introduced an advanced differential hysteretic model for various types of rubber bearings, including laminated rubber bearings (HDRB), lead-rubber bearings (LRB), and natural rubber bearings (NRB) [55]. Adapted from Ozdemir's (1976) elastoplastic model, this method has proved effective for accurately simulating the response of horizontal hysteretic forces in bearing devices, even under complex and dynamic conditions [56].

As expressed by Eq. (15), this model incorporates three equations that together contribute to the evaluation of the horizontal force. The first component involves an elastic nonlinear spring F_1 (refers to Eq. (16)), the second component introduces the hysteretic force in the form of an elastic–plastic spring F_2 (refers to Eq. (18)) while the third comes from a second elastic nonlinear force that accounts for hardening F_3 (refers to Eq. (21)). These elements are outlined in the following equations.

$$F = F_1 + F_2 + F_3 \tag{15}$$

$$F_1 = K_1 \left\{ \beta + (1-\beta)\exp\left(-\frac{U_{\max}}{\alpha}\right) \right\} U + a[1-\exp(-b|U|)]\,\mathrm{sgn}(U) \tag{16}$$

$$U_{\max} = \max(|U(s)|), 0 < s < t \tag{17}$$

$$\dot{F}_2 = \frac{Y_t}{U_t}\left\{ \dot{U} - |\dot{U}| \left|\frac{F_2}{Y_t}\right|^n \mathrm{sgn}\left(\frac{F_2}{Y_t}\right) \right\} \tag{18}$$

$$Y_t = Y_0\left(1 + \left|\left(\frac{U}{U_h}\right)\right|^p\right) \tag{19}$$

$$U_t = U_0\left(1 + \left(\frac{U_{max}}{U_s}\right)\right) \tag{20}$$

$$F_3 = K_2 \left|\frac{U}{U_h}\right|^r U \tag{21}$$

In the aforementioned equations, the U component represents the horizontal relative displacement, F is the total restoring force of the model, and F_i, for $i = 1, 2, 3$, is the internal force of each component. K_1, in Eq. (16), is the initial stiffness of the non-linear elastic spring. The constants α and β are introduced to control the evolution of the stiffness degradation, while a and b control the small strain range and influence the behavior of the nonlinear elastic spring.

The force component related to F_2 presented in Eq. (18), is expressed in a differential component for such a numerical integration is performed providing the solution to calculate its contribution in the form of an elastic–plastic spring force.

The behavior of the third non-linear hardening elastic spring generates the forces in F_3 (refer to Eq. (21)), such is determined by the parameters K_2 (which describes the contribution of the hardening spring) and r (a parameter defining the hardening curve).

In Eqs. (19)–(20), functions Y_t and U_t are explicated as measures of the yield force and the displacement of the elastic–plastic spring, respectively. Both are involved in handling the growth of the area of the hysteresis loop through parameters such as Y_0 (i.e. the initial yielding force), U_H (i.e. the displacement at the onset of hardening), U_0 (i.e. the initial yielding displacement), U_S (i.e. a constant that manages the degradation of elastic stiffness in the elastoplastic spring), and p (i.e. a constant that shapes the hardening trend in the curve).

Table 1
Device ISI S 600/208 P40 Specifications.

Description	Unit	Value
Max. Vertical Load (ULS)	F_{USL} [kN]	2400
Max. Vertical Load (CLS)	F_{CLS} [kN]	1500
Max. deformation (CLS)	d_{ED} [mm]	(±)250
Equivalent Damping	ξ %	16%
Num. Rubber Layers	[-]	26
Thickness of the Rubber Layer	[mm]	8

2.6. Hwang and Wu. Model - Law #6 [57]

Hwang and Wu's analytical model presents an alternative version with a reduced number of parameters compared to Pan and Yang's model [58,59]. It improves the model by incorporating the Mullins effect and the scragging effect in high-damping rubber bearings [60]. In this model, the shear force acting on the bearing is considered as the sum of the restoring force and the damping force.

The model is expressed in the generalized expression provided by Eq. (22).

$$F = F_1 + F_2 \tag{22}$$

$$F_1 = K(x(t), \dot{x}(t))x(t) = \left[a_1 + a_2 x^2(t) + a_3 x^4(t) + \frac{a_4 e^{a_9 \int_0^t F(x(t),\dot{x}(t))\mathrm{d}x(t)}}{\cosh^2\left(a_5 \dot{x}(t)\right)} \right] x(t) \tag{23}$$

$$F_2 = C(x(t), \dot{x}(t))\dot{x}(t) = \frac{a_6 + a_7 x^2(t)}{\sqrt{a_8^2 + \dot{x}^2(t)}} \left(1 + e^{a_{10}\int_0^t F(x(t),\dot{x}(t))\mathrm{d}x(t)}\right) \dot{x}(t) \tag{24}$$

In this context, F is the shear force transmitted by the bearing, which consists of the restoring force F_1 and the damping force F_2.

$K(x(t); x'(t))$ depicted in Eq. (23), represents the stiffness of the bearings, while $C(x(t); x'(t))$,introduced in Eq. (24), is the damping coefficient. Both stiffness and damping coefficient depend on the relative displacement ($x(t)$) and Velocity ($\dot{x}(t)$) input.

In Eq. (23), the terms a_1, a_2 and a_3 refer to the restoring force of the device. In the same equation, a_4 and a_9 account for stiffness degradation due to cyclic softening of the hysteretic loop associated with the Mullins and Scragging effects.

For the damping force, Eq. (24) contains the parameters a_6, a_7, and a_8 which control the behavior of this component. Combining these parameters with a_{10} and the integral representing the energy dissipated by the elastomer during cyclic loading helps to manage the reduction in loop area.

3. Description of the laboratory tests

SISMALAB s.r.l. laboratory conducted an experimental survey with the aim to certificate a mass-production series of devices realized from 2021 to 2023. During the campaign, randomly selected samples were tested from batch production lots. The purpose of this testing was to ensure that such devices met serviceability and performance standards according to the Italian national code and government regulations.

During this period, over 160 elastomeric isolators from the ISI-S 600/208 P40 series were tested. As depicted in Figs. 1 and 2, these devices feature alternating layers of rubber bonded together through a vulcanization process. This layered construction guarantees high bearing capacity and sufficient horizontal deformation, achieving the desired damping (i.e. dissipation capacity) during their service life. Notably, the device employs a "Soft" rubber compound that provides a shear modulus of $G = 0.4$ MPa, observed during the mechanical test.

The properties and design performance for ISI-S 600/208 P40 series are presented in Table 1.

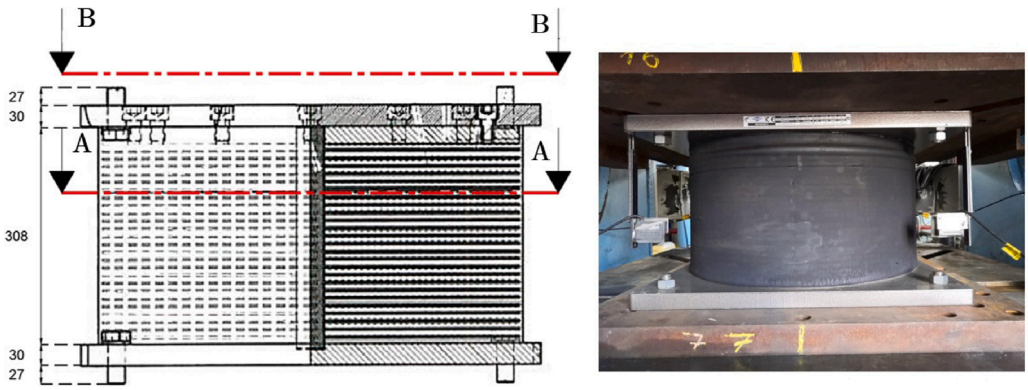

Fig. 1. Technical Drawings device ISI-S 600/208 P40 (left) and *Test on Second Lot Sampling FPC 2022 Device 8265. All units are expressed in* [*mm*] (right).

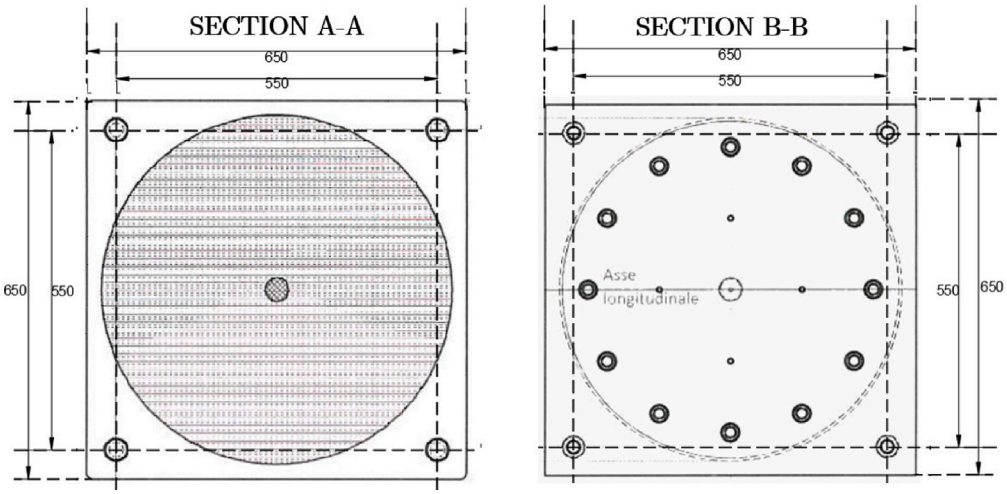

Fig. 2. Sections device ISI-S 600/208 P40 - All units are expressed in [mm].

Table 2
Test Denomination Specifications.

Test Denomination	Displacement [mm]	Displacement [%]	Frequency [Hz]	V. Load [kN]	Waveform	Cycles
H.C.C. Test	208	100%Tq	0.5	1632	Sine	3

The cyclic tests were performed with a hydraulic cylinder controlled by pressure transducers. It applies a constant vertical load of 6 MPa (1632 kN) to the sample. Additionally, horizontal movement is managed by a hydraulic cylinder, either using a position transducer located near the piston rod or a load cell positioned at the end of the piston rod. All the data provided by the transducers have been collected and processed by the Sisma-Control software (Fig. 3).

To record the cyclic forces, a load cell was positioned between the actuator and the HDRB specimen, while a transducer monitored the device's movements. These specimens were tested on a displacement-imposed test, the movements were controlled by a transducer mounted on the device. The control and data acquisition system allowed for real-time analysis of device displacements by instantly adjusting applied forces via the hydraulic pressure system's automatic control. The displacement-time history followed a sinusoidal pattern.

The test protocol followed by the laboratory was performed according to UNI EN 15129–8.2.1.2.2 [61]. Specifically, horizontal Characteristics under Cyclic deformation (H.C.C) were tested. In Table 2 the details of the test are presented. Additionally, the experimental displacement retrieved by the equipment during the execution of the 3-cycle input for Sample n°8317 of Lot n°2 is presented in Fig. 4.

Test results of ten isolators were randomly selected from those tested with the same characteristics, provided by the SISMALAB laboratory, as representative of the entire stock. Preliminary data cleaning was carried out to remove intrinsic noise, particularly in the deformation collected by the testing equipment. The observed scattering in the displacement data was linked to tremors detected by the sensor during the load application stages. Signal cleaning was effectively performed using a moving average filter.

4. Identification framework

In this section, the mathematical formulation for the optimization problem is introduced. This includes the definition of the objective function (OF) and the design variable. Consequently, the optimization process's criteria and the implementation of the GA are outlined.

4.1. Mathematical formulation and analysis setting

The parameter identification requires solving an unconstrained optimization problem where a suitable objective function (OF) has to be minimized.

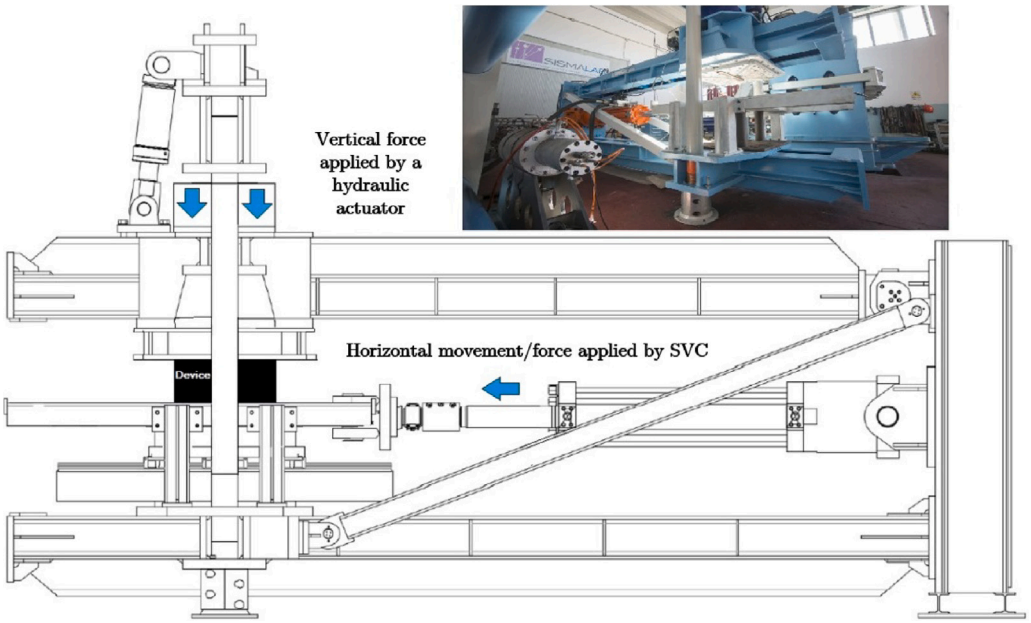

Fig. 3. Test Equipment at SISMALAB: ISOL 1000.

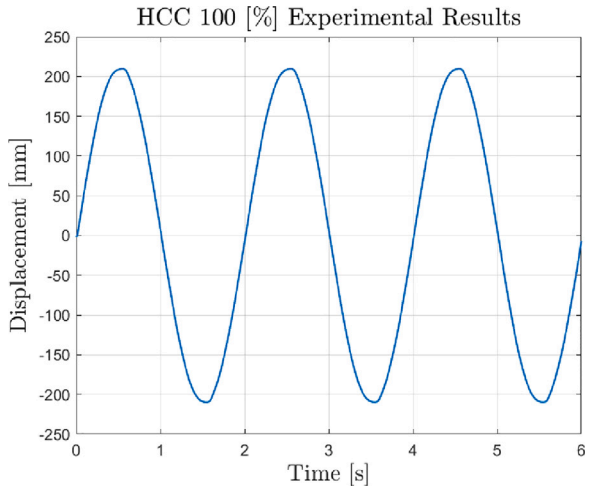

Fig. 4. HDRB Device n°8317 of Lot n°2 Experimental displacement [mm] VS time [s].

The numerical output of each law depends on different parameters, which represent the component of the design variable vector x. The model parameters are identified by solving the following single-objective optimization problem:

$$\textbf{Minimize} \quad W = f(x) \tag{25}$$

$$\textbf{Subject to} \quad x_i^l \le x_i \le x_i^u \tag{26}$$

where $x = \{x_1, \dots, x_i, \dots, x_n\}$ represents a set of real parameters which depends on the case-by-case numerical model. The size of this vector, hence, is related to the number of variables which govern the constitutive law. The $x^l = \{x_1^l, \dots, x_j^l, \dots, x_n^l\}$ and $x^u = \{x_1^u, \dots, x_j^u, \dots, x_n^u\}$ vectors represent the lower and upper bounds of x_i, respectively. In this way, the domain of feasible solutions is restricted to a sub-domain in which x_i can assume the values between x^l and x^u.

For the aim of this research, a suitable OF has been defined in the integral form as follows:

$$f(\mathbf{x}) = \frac{1}{\sigma_{p_m}(t_{end} - t_{start})} \int_{t_{start}}^{t_{end}} abs(p_m - p_e(x))dt \tag{27}$$

where t_{start} and t_{end} are the start and end time records, respectively, and $p_m(t)$ is the experimentally measured force, while $p_e(t)$ is the estimated force [62].

The Matlab [63] ODE45 function has been used for solving the (nonstiff) ordinary differential problem. The procedure implemented by the solver is the Runge–Kutta method. The fixed time step for the solution procedure is the sampling time step adopted during the laboratory test. This procedure was adopted for only the differential laws (from law #4 up to law #6)

To reduce the computational effort during the optimization process or avoid numerical instabilities during the computation, lower, x^l, and upper, x^u, bounds for each design variable are carefully fixed, detecting more suitable ranges of variability. In this way, unfeasible solutions are neglected, and the efficient exploration phase of the algorithm is guaranteed [64].

In order to solve the problem stated in the previous section, a real-coded GA is adopted.

A population size of 100 individuals and a maximum number of iterations equal to 50 has been fixed. No. 20 independent runs have been performed to investigate the robustness of the optimization process and analyze the variability of the OF as well as the parameters of each law for each (Table 3).

Once the initial population has been initialized, through the random definition of the chromosome and the assignment of the fitness value for each individual, the fitness of each individual is calculated in terms of the difference between experimental input and numerical output expressed by Eq. (27). Each design variable is free to range within the interval defined by the lower and upper bounds shown in Table 4. Following the traditional strategies of the Genetic Algorithm, the parent selection is performed through the Roulette Wheel [65], and a number of children equal to that of the parents is generated by a Double Point Crossover [66]. A uniform random mutation is performed with an activation rate of 1% [67]. At the end of the process, the best solution is selected and the optimal set of parameters that govern that specific law is detected.

Table 3
Setting criteria GA for each Numerical Law.

Pop.Size	N.Generation	Evaluation	N. Runs	Stagnation
100	50	5000	20	0.05

Although a maximum number of iterations of 50 has been set, the stop criterion occurs if the OF remains unchanged for at least 20 subsequent iterations. In this way, the computational effort is reduced if stagnation is recognized.

The optimization processes were run on a workstation DELL - Precision 7680 with an Intel Core i7 5,3 GHz processor with 32 GB RAM under the Microsoft Windows 11 operating system. The computational time for each run over 20 devices varies from about 241.5 s, for simplest algebraic models (i.e. Bilinear), up to 14'852.8 s for the most computationally demanding differential ones (i.e. Bouc Wen).

5. Parameter identification results and cyclic behavior reproduction

This section presents the results obtained from the investigated numerical models, focusing on their effectiveness in replicating the experimental input. In Fig. 5, comparisons between experimental hysteretic force vs displacement cycles and numerical outputs for device 4 are selected among all the tests since it represents the best performer of the series. In Appendix, the mean and standard deviation over 20 runs of the design variables and objective functions of each law for all tested devices are reported for completeness reasons.

All the numerical models show an acceptable level of accuracy and efficiently simulate the experimental trend of the cycles. However, by observing Fig. 5(a), the Bilinear model fails to capture the smooth transition within the cycles for lower and higher levels of deformation. On the other hand, the inner properties of the Jankowski and Vaiana models, shown in Fig. 5(b)–(c), excel in reproducing all the cycles, especially the initial one, accurately fitting the slope that represents the stiffness of the first graph branch. Especially, the Jankowski algebraic model exhibits a higher level of match with the experimental cycles thanks to a significant improvement in reproducing the stiffness variation, at the maximum imposed deformation, and the trend of the final unloading cycle. The most important loss of accuracy comes from the inability to reproduce the pinching phenomenon occurring at low deformation rates.

With specific regard to the response of the differential laws, shown in Fig. 5(d)–(f), all models show improved smooth transitions between the elastic and elasto-plastic branches, as well as better curve fitting in the ascending and descending branches of the graphs. This behavior enables an accurate simulation of the HDRB response under the given input. However, this is obtained at the cost of increased computational demand due to the calculation of solving nonstiff differential equations embedded within these laws.

The Bouc-Wen model (Fig. 5(d)) and the Abe et al. model (Fig. 5(e)) exhibit similar numerical force responses for the device. This similarity arises from their shared mathematical foundation. However, the Abe et al. model incorporates improved considerations for degradation effects.

The Hwang and Wu model (Fig. 5(f)) shows satisfactory performance in the larger repetitive cycles. However, compared to the other two laws in this differential category, it poorly calibrates the first cycle. The model prioritizes the calculation of overall stiffness in the most repetitive cycles, neglecting the initial data progression.

It is worth noting that the nature of the experimental input, characterized by serviceability tests conducted at low deformation levels and low input cycles at low frequency, cannot fully exploit the degradation, pinching or post-hardening ability of the differential models like the adopted ones. The performance of these models could be more evident with experimental tests conducted for larger displacement and higher deformation rates of the device.

Finally, the error of the calibration, calculated for each law over 10 devices and 20 runs, is below 10% for all models, except the Bilinear law. Increasing the number of Populations, Generations, or simulation cycles has been found to have no effect on the convergence of the exploration variables poorly affecting the overall accuracy of the investigated models. At this stage of the investigation, the Jankowski model emerges as the best overall choice both in terms of computational efficiency and goodness of the numerical output. In the next section, the comparison between these models will be conducted based on a statistical analysis of the overall performance of each model and the variability of their parameters.

Table 4
Lower and upper bounds of the models' parameters.

Law	Parameter	Lower Bound (X_l)	Upper Bound (X_u)
Law #1	K_1 [kN/mm]	1	1.9
BiLinear	K_2 [kN/mm]	0.35	0.95
Model	F_y [mm]	30	80
Law #2	a_1 [N/m]	10^4	10^6
Jankowski	a_2 [N/m^3]	10^6	9×10^6
Model	a_3 [N/m^5]	10^6	9×10^6
	a_4 [N/m]	10^3	10^5
	a_5 [s/m]	10^3	10^4
	a_6 [N/m]	10^5	3.5×10^6
	a_7 [s/m]	0	10
	a_8 [1/m]	5	20
	a_9 [N]	10^4	10^5
	a_{10} [N/m^2]	10^4	10^5
	a_{11} [m/s]	0	10
Law #3	K_{b+} [N/m]	10^5	6×10^5
Vaiana	K_{b-} [N/m]	10^5	6×10^5
Model	F_{0+} [N]	10^4	10^5
	F_{0-} [N]	10^4	10^5
	α_+ [1/m]	0	50
	α_- [1/m]	0	50
	β_{1+} [N]	0	0.9
	β_{1-} [N]	−0.9	0
	β_{2+} [1/m]	15	50
	β_{2-} [1/m]	−50	−15
Law #4	α [-]	0.1	0.2
BoucWen	Ke [kN/mm]	2	4
Model	A [-]	1	2
	β [1/mm]	0.025	0.075
	n [-]	1	1.25
	γ [1/mm]	0.025	0.075
Law #5	K_1 [kN/mm]	5	10
Abe. et. al.	α [mm]	0	10
Model	β [-]	0.01	1
	a [kN]	0.5	1
	b [1/mm]	5	10
	n [-]	0.01	0.5
	Y_0 [kN]	10	70
	X_h [mm]	50	150
	p [-]	0.01	2
	X_0 [mm]	2	6
	X_s [mm]	5	50
	K_2 [kN/mm]	0.01	0.5
	r [-]	0.01	0.2
Law #6	a_1 [-]	2.8×10^3	8.9×10^3
Hwang Wu	a_2 [-]	−5	−0.04
Model	a_3 [-]	1×10^{-4}	0.01
	a_4 [-]	20.75	90
	a_5 [-]	1×10^{-3}	0.9
	a_6 [-]	10^4	1.5×10^5
	a_7 [-]	1	8
	a_8 [-]	50	150
	a_9 [-]	-5×10^{-6}	-1×10^{-9}
	a_{10} [-]	-2.925×10^{-5}	0

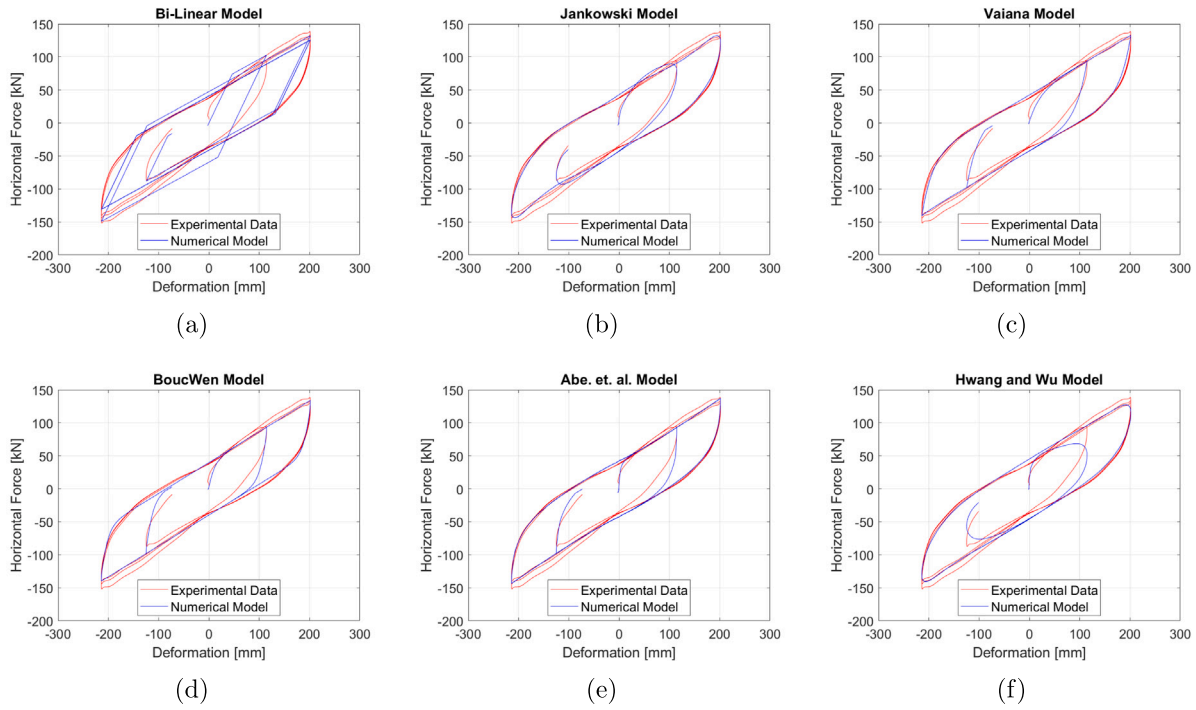

Fig. 5. Comparison between experimental and numerical force–displacement relationships for the algebraic model (refers to law #1 (a), law #2 (b)), transcendental model (refers to law3 (c)), and differential ones (refers to law #4 (d), law #5 (e), law #6 (f)) with specific regard to Device #4 Test #20.

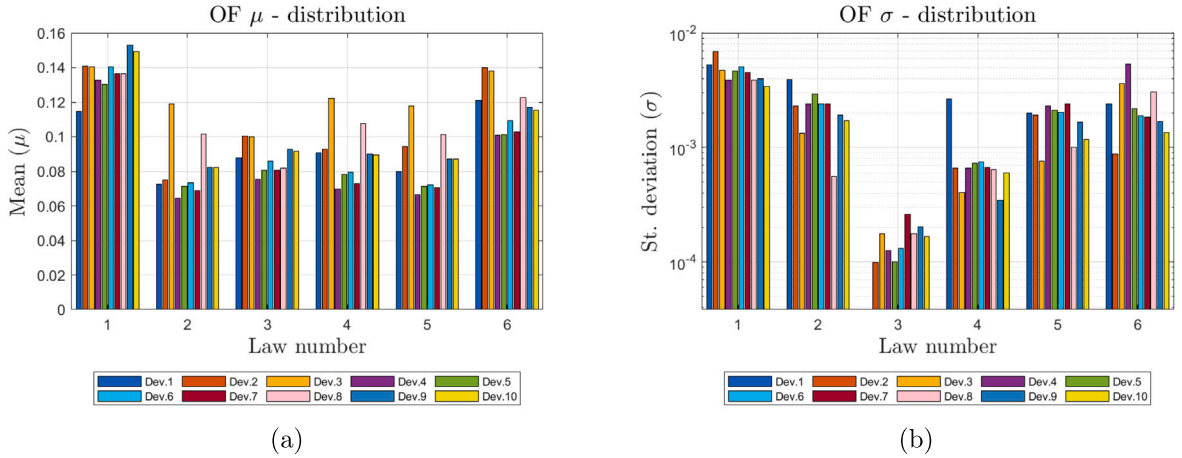

Fig. 6. OF mean (μ) distribution for each test devices (a); OF standard deviation (σ) distribution for each test devices (b). For each law, ($X-axis$), different colors are used for detecting the corresponding device.

6. Statistic analysis and discussion

The gathered data from the optimization process for the selected numerical models have been analyzed to uncover inherent trends and patterns.

Fig. 6 illustrates the bar graphs depicting the mean distribution and standard deviation of the OF for each device across six numerical hysteresis models based on the results obtained from 20 independent runs. In other words, the graphs showcase the accuracy (Fig. 6(a)) of the models in replicating laboratory tests and their robustness (Fig. 6(b)). More in detail, Fig. 6(a) underscores the numerical model's capability of minimizing discrepancies between the observed experimental behavior and the optimal numerical solution. A lower OF value for a given numerical model indicates that the corresponding model effectively aligns with the experimentally measured force because of its efficient adaptability through a suitable tuning of its parameters.

Among all the investigated models, law #2 (algebraic) and law #5 (differential) are identified as the most accurate models, closely followed by laws #4 (differential) and #3 (algebraic) which are also characterized by a limited variability of the OF between the devices.

Fig. 6(b) allow to rank models through the variability of the OF values over 20 runs observed for each device of the series. To highlight the variation trend of the standard deviation σ across the examined laws, a logarithmic scale is employed. With respect to the other models, law #3 shows dispersion values with an order of magnitude smaller. Additionally, it is characterized by the lowest variability among the series devices' OF.

Fig. 7 provides further insights properly related to the variability of the OF values, evaluated as the mean value over 20 runs, of each device with respect to the average (i.e. dotted line) over the 10 devices of each law. The model with OF values closer to the mean value gives a measure of the level of influence of the production series on the variability of the numerical output.

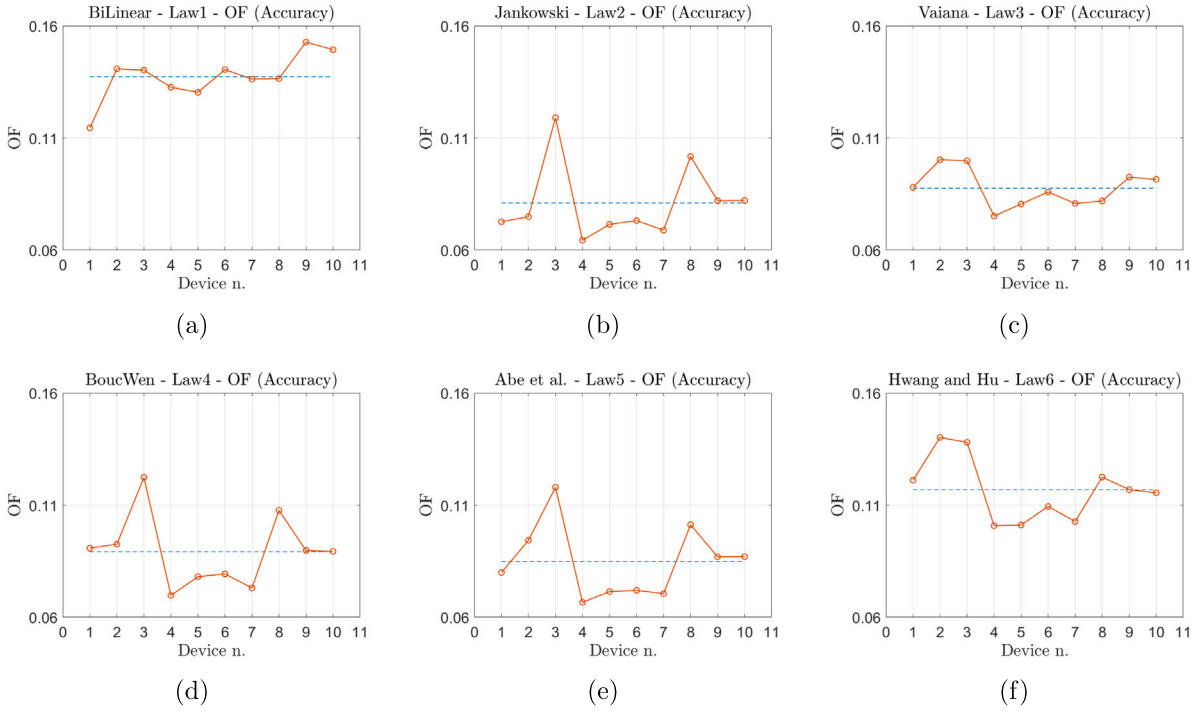

Fig. 7. OF mean (μ) values for each device considering 20 independent runs for each device and each law. The dotted line represents the mean values calculated over the 10 devices.

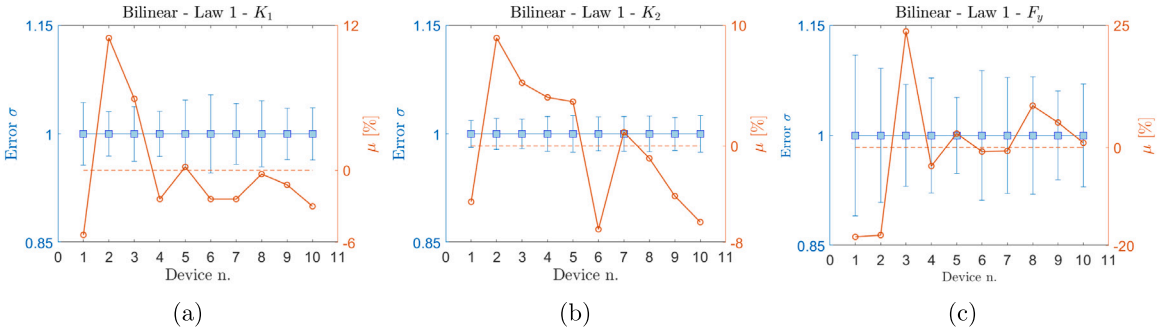

Fig. 8. Normalized standard deviation and mean distribution of the identified K_1 (a), parameter K_2 (b) and F_y (c) for law #1. The left $y-axis$ shows the error bar of the standard deviation (σ), while the right $y-axis$ the percentage variation of mean distribution (μ). The dotted line represents the mean reference value among all ten mean values evaluated for each device.

Even if, laws #2 and #5 emerge as the most accurate solutions with the lowest OF values approaching 6% of discrepancy with respect to the experimental input; the lowest dispersion over 10 devices is achieved for laws #3 and #4, closely followed by law #5.

Specifically, device #4 best fits all laws showing the highest level of accuracy except Law #1. In the same way, devices #4, #5, #6, #7 exhibit consistent behavior across laws, indicating reliability in terms of expected performance regardless of the adopted numerical law. Finally, devices #2, #3, and #8 exhibit notable variability in terms of expected accuracy results associated with a specific law.

All the considerations so far focused on analyzing the global accuracy and robustness of the investigated models. However, aiming to identify the parameter which mostly affects the variability of a specific law, further analysis will be devoted to the assessment of the degree of parameters' dispersion related to each law. This approach enables the evaluation of which parameter predominantly influences the overall robustness.

For each law, the influence of the parameters is analyzed in terms of normalized dispersion as well as the percentage mean variation as reported in Figs. 8–13. These figures present the statistics of the identified parameters for the various adopted models and devices. Each graph exhibits a dual vertical axis: on the left, the standard deviation of the considered parameter relative to the mean of all runs for each device (error bar of the standard deviation - $Error\ \sigma$) is depicted, while on the right axis, it illustrates the percentage variation of the mean of the considered parameter (computed over the range of 20 optimization runs) compared to the reference mean value (indicated by the red dotted line), which is evaluated as the mean of all mean values for each device. In other words, the former mostly gives information about the variability of the parameters over the optimization runs while the latter offers insights related to the variability of the same parameters over the devices of the production series.

Similar trends can be detected by observing the statistical results collected for each law. More in detail, each law has a parameter with an error σ distribution and a percentage variation μ which dominate the other ones. For law #1, F_y achieves a peak of σ equal to almost 1.15 for all the devices and a variation of μ with respect to the reference average value around 20%–25% for devices #1, #2 and #3 (see Fig. 8(c)). The physical interpretation for the variation in F_y could be attributed to the possible variability in the rubber mix, since it correspond to

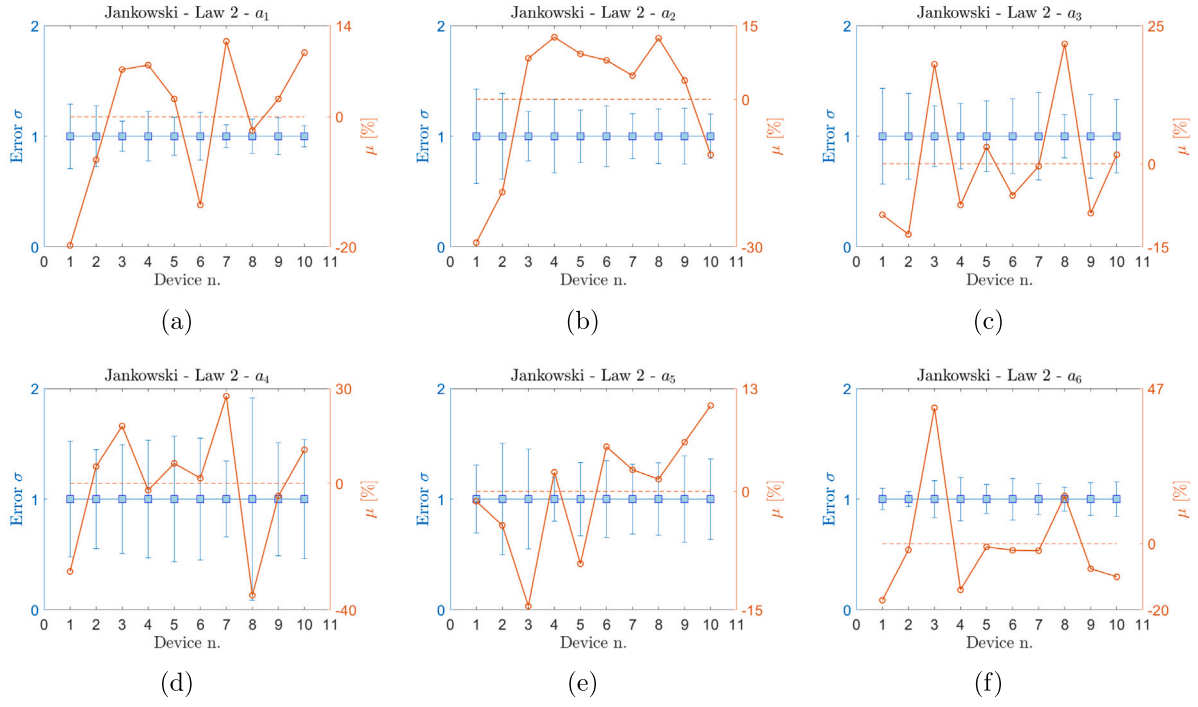

Fig. 9. Normalized standard deviation and mean distribution of the identified a_1 (a), a_2 (b), a_3 (c), a_4 (d), a_5 (e), a_6 (f), a_7 (g), a_8 (h), a_9 (i), a_{10} (j) and a_{11} (k) for law #2. The left $y-axis$ shows the error bar of the standard deviation (σ), while the right $y-axis$ the percentage variation of mean distribution (μ). The dotted line represents the mean reference value among all ten mean values calculated over 20 runs for each device.

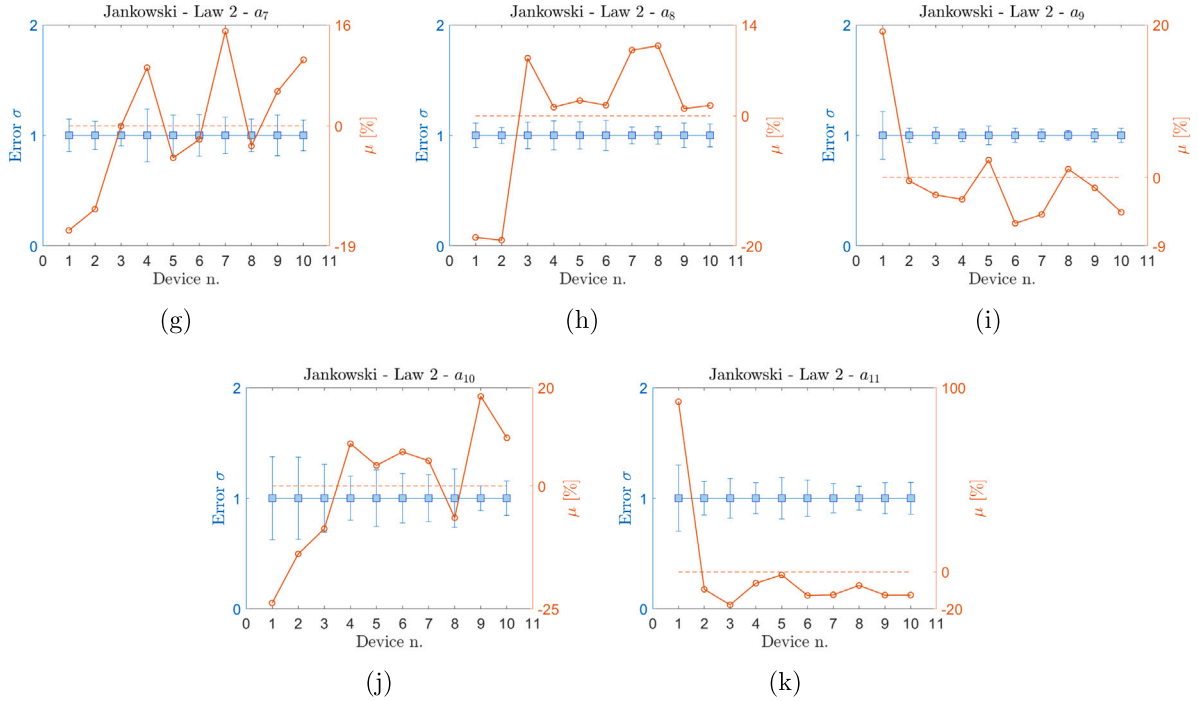

Fig. 9. (*continued*).

different batch and lots, maybe it is interesting to mention that. In the Jankowski model parameter a_4 (see Fig. 9(d)) exhibits a maximum σ of 2.0 for device 8 while the same parameter maintains a significant dispersion around 1.5 for the other devices. For the same parameter, it is observed a significant dispersion also in terms of μ with a peak of discrepancy around 40%, with respect to the reference average value. The Maximum dispersion reaches 47% and is found in parameter a_7 (see Fig. 9(f)). Even if parameter a_{11} (see Fig. 9(k)) is generally characterized by a low dispersion of the μ over the samples series, for device 1 a deviation of almost 100% can be recognized. For the Vaiana model, parameters β_{1+} and β_{1-} have the highest dispersion which is generally the same for all the devices as depicted in Fig. 10(g)–(h), respectively. For such parameters, the same trend is also confirmed in terms of μ even if β_{2-} (see Fig. 10(j)) shows a huge dispersion over all the devices. On the other hand, the same parameter has a low σ for each device with respect to the previous ones.

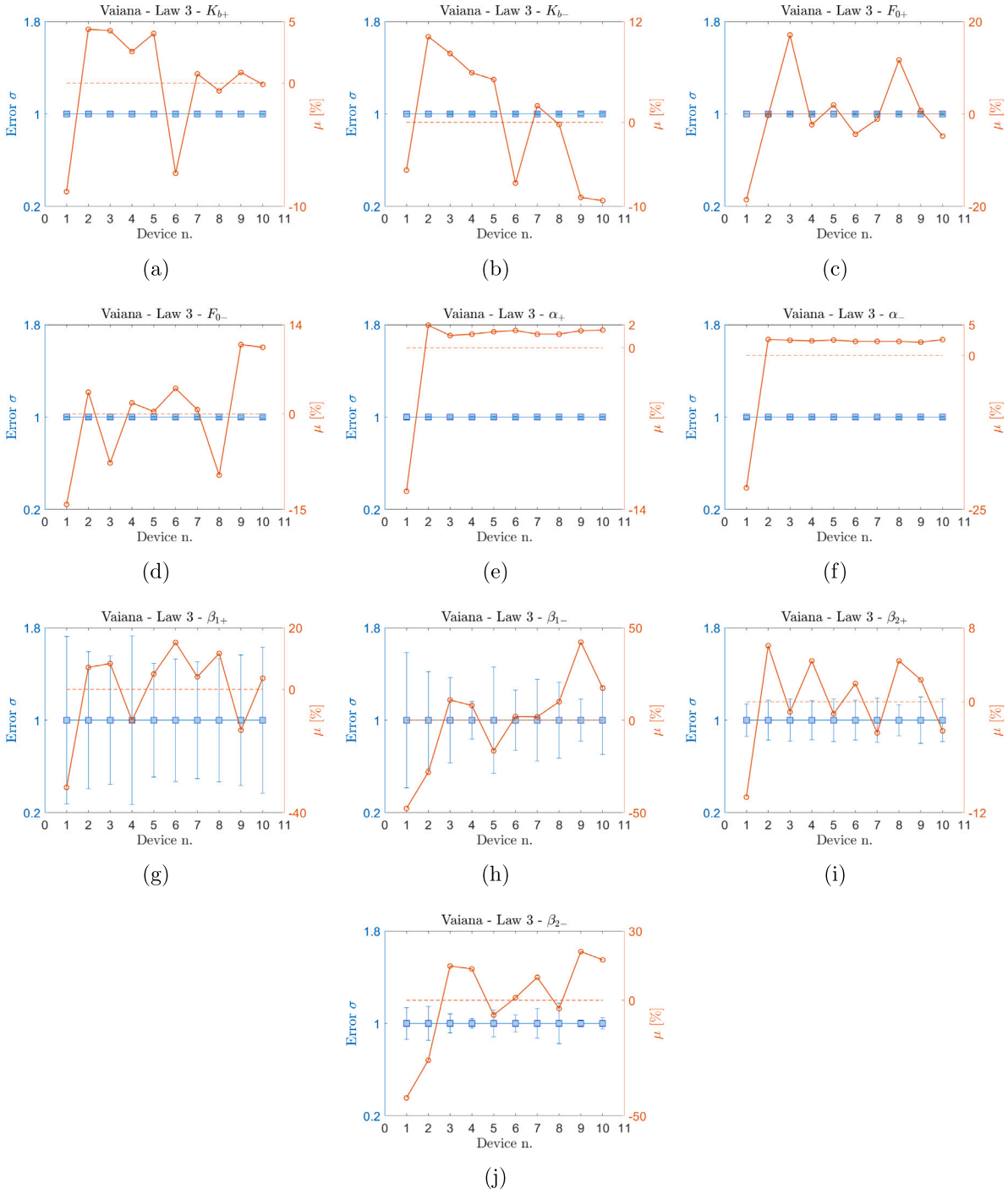

Fig. 10. Normalized standard deviation and mean distribution of the identified K_{b+} (a), parameter K_{b-} (b), parameter F_{0+} (c), F_{0-} (d), α_{+} (e), parameter α_{-} (f), parameter β_{1+} (g) and β_{1-} (h), β_{2+} (i) and β_{2-} (j) for law #3. The left $y-axis$ shows the error bar of the standard deviation (σ), while the right $y-axis$ the percentage variation of mean distribution (μ). The dotted line represents the mean reference value among all ten mean values calculated over 20 runs for each device.

With specific regard Bouc Wen model, the highest variability over the runs is given by parameters A and γ (see Fig. 11(c)–(f)) while β has the highest percentage deviation of μ as reported in Fig. 11(d). In law #5, parameters α, n and r dominate the other ones both in terms of error σ and μ as shown in Fig. 12(b)–(f). Finally, Hwang and Hu model is characterized by a low dispersion, over the runs as well as along the devices, of all the parameters with the exception of parameter a_{10} (see Fig. 13(j)) which exhibits a maximum value of σ and μ equal to 5 and 200, respectively.

From a generic point of view, it is evident that device #1 represents the outsider among the other devices of the series with a significantly high value of μ independent of the considered law. It indicates an underlying issue with the behavior of the isolator. On the other hand, disregarding Bilinear law, devices #9 and #10 are the less sensitive with respect to the considered numerical models with a level of accuracy always close to the average mean value calculated over the 10 devices and 20 runs (refers to Fig. 7). Additionally, when the dispersion σ over the runs is concentrated on one or a few parameters of a specific law, such dispersion can be observed along all the production series with slight differences among the devices. In other words, the high dispersion over the optimization runs of specific parameters is independent of the considered device while a clear relationship between the

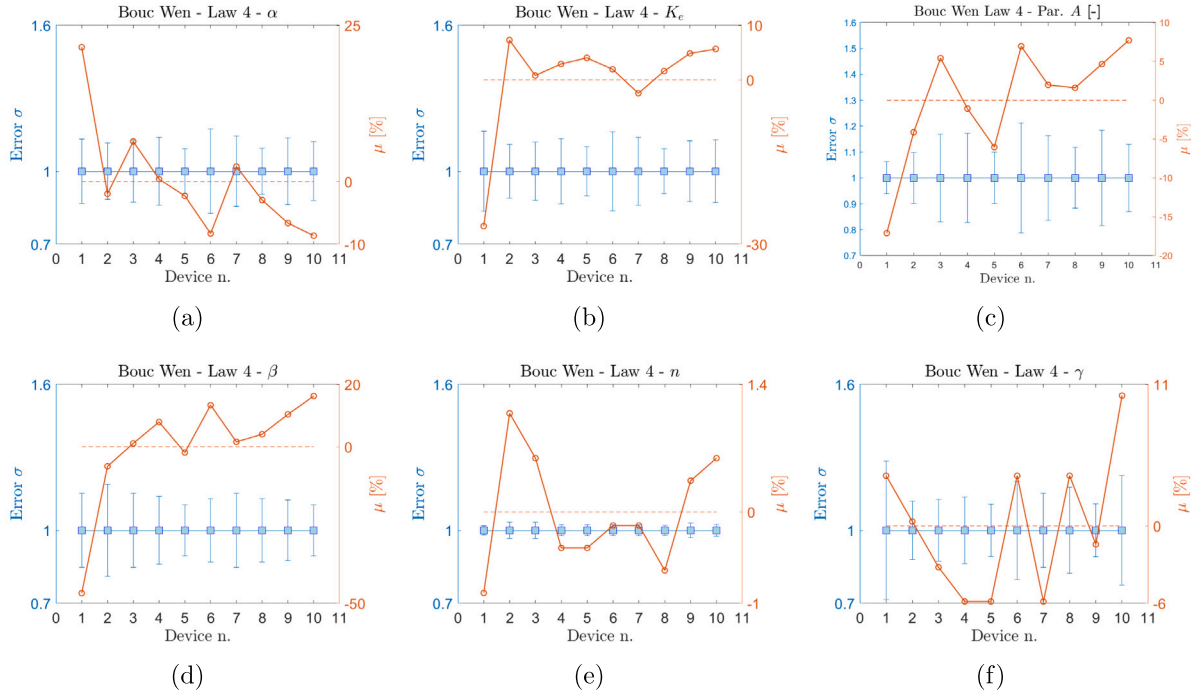

Fig. 11. Normalized standard deviation and mean distribution of the identified α (a), parameter Ke (b), parameter A (c) and β (d), n (e) and γ (f) for law #4. The left $y-axis$ shows the error bar of the standard deviation (σ), while the right $y-axis$ the percentage variation of mean distribution (μ). The dotted line represents the mean reference value among all ten mean values calculated over 20 runs for each device.

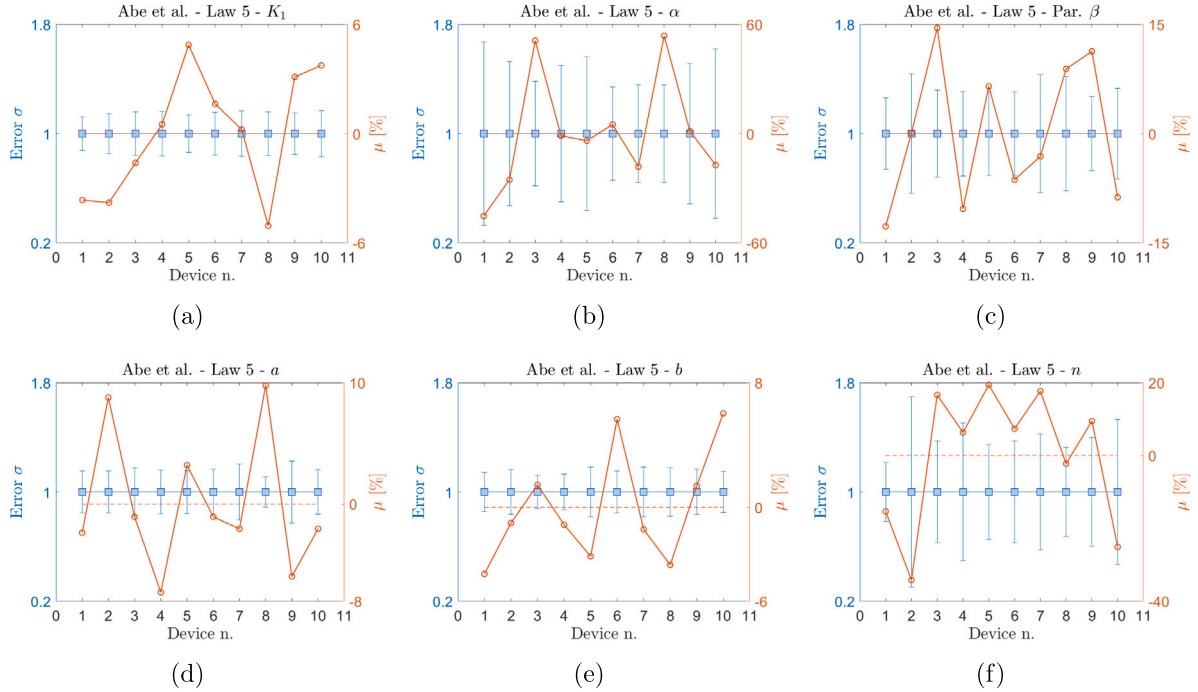

Fig. 12. Normalized standard deviation and mean distribution of the identified K_1 (a), α (b), β (c), a (d), b (e), n (f), Y_0 (g), X_h (h), p (i), X_0 (j), X_s (k), K_2 (l) and r (m) for law #5. The left $y-axis$ shows the error bar of the standard deviation (σ), while the right $y-axis$ the percentage variation of mean distribution (μ). The dotted line represents the mean reference value among all ten mean values calculated over 20 runs for each device.

proper device and the investigated parameter can be highlighted when considering the variability of such parameter along the production series in terms of μ.

Finally, the robustness of algebraic laws is inversely proportional to the complexity of the model. It can be observed that as the law number increases from law #1 (Bilinear Model) to law #3 (Vaiana Model), the parameters' dispersion for the model decreases, indicating that as the complexity of algebraic laws increases, the model becomes more robust.

In contrast to the algebraic laws, the robustness of differential laws decreases as complexity increases, moving from the Bouc Wen Model (law #4) to the Abe et al. Model (law #5), and finally to the Hwang and Wu Model (law #6). This is evident from the increased OF dispersion among the devices. In terms of accuracy, the Abe et al. Model (law #5) demonstrates the highest precision among the differential laws,

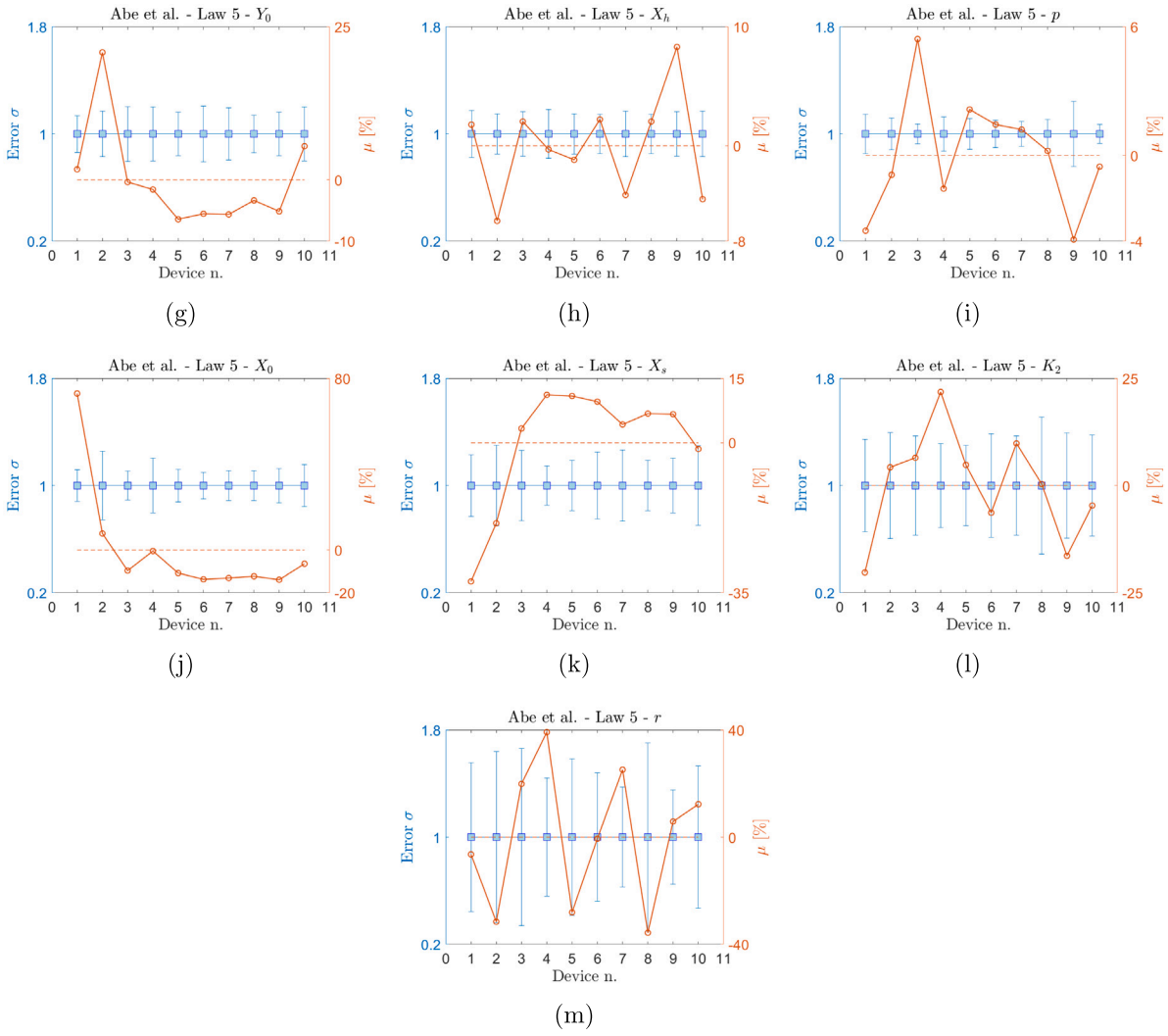

Fig. 12. (*continued*).

followed closely by the Bouc Wen Model (law #4). The Hwang and Wu Model (law #6) has the highest mean error in the OF.

7. Pareto front representation

In this section, the authors point out mathematical considerations to identify the best performer among the investigated models. In the previous Section 6, the effect of the variability of the parameters on the overall accuracy (OF) and robustness (σ) has been treated separately. However, the final scope of this research passes through the identification of the best performer able to efficiently reproduce the experimental input of each device guaranteeing a good level of reliability along all the tests of the production series. If the former can be still assumed as representative of the global capability of a model to fit with experimental outputs, the latter gives a measure of how a single parameter can affect a specific model without any information about the overall robustness of that model.

To achieve this goal, the authors introduce a new robustness indicator, called β index, in order to give a measure of the reliability or, in other words, a measure of the global level of dispersion of each investigated model. In the following, the mathematical procedure for its calculation is introduced.

At first, a matrix representation of parameters set for each law is derived in the following form:

$$\boldsymbol{\alpha} = \left(\begin{bmatrix} \alpha_{11}^{(1)} & \alpha_{12}^{(1)} & \dots & \alpha_{1n}^{(1)} \\ \alpha_{21}^{(1)} & \alpha_{22}^{(1)} & \dots & \alpha_{2n}^{(1)} \\ \vdots & \vdots & \vdots & \vdots \\ \alpha_{m1}^{(1)} & \alpha_{m2}^{(1)} & \dots & \alpha_{mn}^{(1)} \end{bmatrix} \begin{bmatrix} \alpha_{11}^{(2)} & \alpha_{12}^{(2)} & \dots & \alpha_{1n}^{(2)} \\ \alpha_{21}^{(2)} & \alpha_{22}^{(2)} & \dots & \alpha_{2n}^{(2)} \\ \vdots & \vdots & \vdots & \vdots \\ \alpha_{m1}^{(2)} & \alpha_{m2}^{(2)} & \dots & \alpha_{mn}^{(2)} \end{bmatrix} \dots \begin{bmatrix} \alpha_{11}^{(j)} & \alpha_{12}^{(j)} & \dots & \alpha_{1n}^{(j)} \\ \alpha_{21}^{(j)} & \alpha_{22}^{(j)} & \dots & \alpha_{2n}^{(j)} \\ \vdots & \vdots & \vdots & \vdots \\ \alpha_{m1}^{(j)} & \alpha_{m2}^{(j)} & \dots & \alpha_{mn}^{(j)} \end{bmatrix} \right) \tag{28}$$

Vector α collects all parameters ($\alpha_{m,n}$) in matrices. Each matrix is representative of a specific law (j). Pedix m represents the different samples while pedix n stays for the different parameters depending on the specific law (apex j).

At first, percentage variations of each parameter, with respect to a reference value, are evaluated for each considered law. For example, the percentage variation, $\Delta_1^{(j)}$, of the parameter $n = 1$ of the generic constitutive law j will be written as following:

$$\Delta_1^{(j)} = max(abs(\{\Delta_{11}^{(j)}, \Delta_{21}^{(j)}, \dots, \Delta_{m1}^{(j)}\})) \tag{29}$$

$$\textbf{where} \quad \Delta_{m1} = \frac{\alpha_{m1} - \alpha_{\mu 1}}{\alpha_{\mu 1}}. \tag{30}$$

This procedure is applied for each parameter of each investigated constitutive law. In this way, for the generic law j, the value β_j can

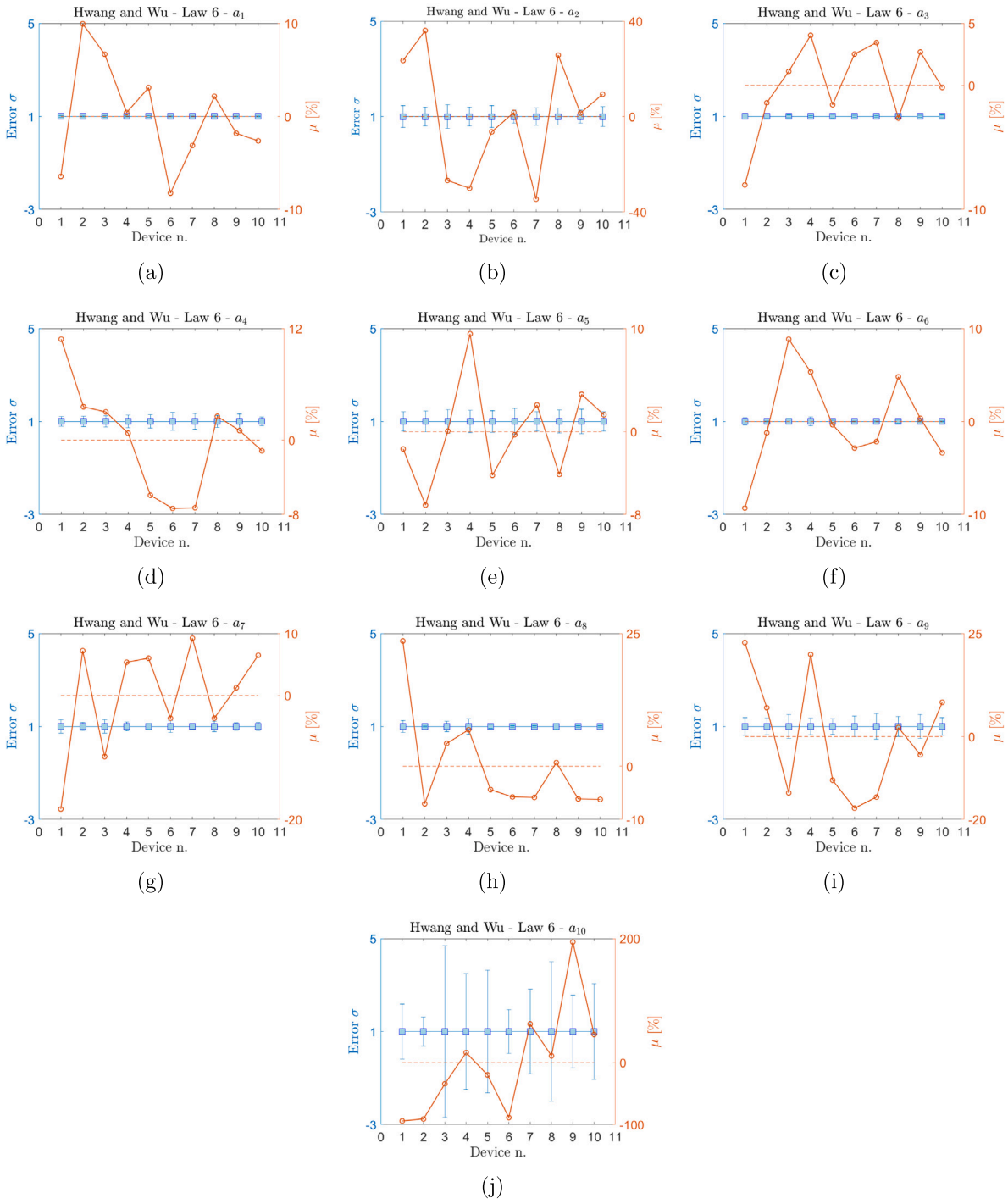

Fig. 13. Normalized standard deviation and mean distribution of the identified a_1 (a), parameter a_2 (b), parameter a_3 (c) and a_4 (d), a_5 (e), parameter a_6 (f), parameter a_7 (g), a_8 (h), a_9 (i) and a_{10} (j) for law #6. The left $y-axis$ shows the error bar of the standard deviation (σ), while the right $y-axis$ the percentage variation of mean distribution (μ). The dotted line represents the mean reference value among all ten mean values calculated over 20 runs for each device.

be evaluated as:

$$\beta_j = \frac{\sum \Delta_n^{(j)}}{n_n}. \tag{31}$$

The no-dimensional value β can be assumed as a robustness index corresponding to the generic law j. This value is obtained, for each law, by summing all the percentage variations of the n parameter which govern that specific constitutive law.

Aiming to provide further insights concerning the specific simulating properties of the investigated models, a Pareto from representation is reported in Fig. 14. Thanks to this graphical representation, an efficient assessment procedure for the evaluation of the best performers is developed ranking the constitutive models according to the goodness of the numerical models to reproduce the experimental results within the design limits considering reliability and accuracy qualities.

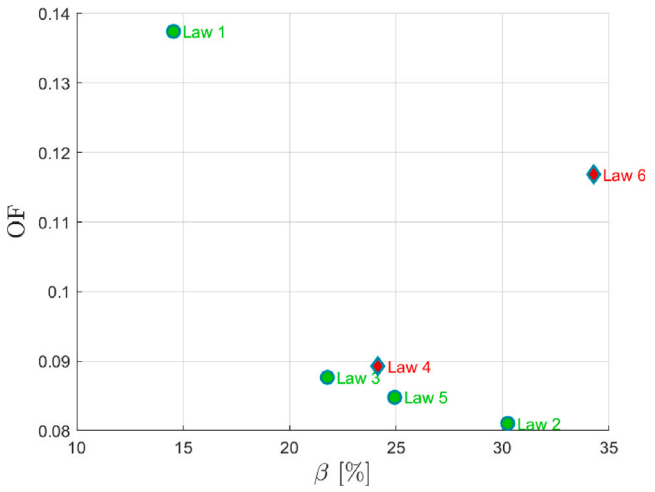

Fig. 14. Accuracy (OF) vs robustness (β) Pareto front. The best constitutive laws as a good compromise between accuracy and robustness are marked in green while the dominated solutions are reported in red. The trend realized by connecting the green points represents the Pareto front of the non-dominated solutions.

It depicts the OF parameter, evaluated as the mean of all twenty optimization runs and among all devices, and index β on the Y and X-axis, respectively. Increasing the accuracy of a model (lower values of OF), a decrease in the overall robustness (high values of β accounting for an increase of dispersion) is observed. Due to the opposite trend of these indices, a Pareto Front plot is developed and the best performer among all investigated models is identified.

In the scatter representation, data are clustered into two groups by using green and red colors. Green points represent the good compromise between accuracy and robustness features, while red points are the dominated-solution of the optimization problem. In other words, by selecting one of the red-marked points, it is always possible to identify whatever solutions, among the green ones, which can be preferred in terms of accuracy or robustness (or both).

The set of optimal solutions populating the Pareto front represents the best compromise between the accuracy of the model, OF, and its robustness, β.

8. Conclusions and future developments

In the present paper, an identification procedure for the evaluation of the optimal parameters of six different HDRB numerical models has been implemented. Data derived from an experimental campaign has been adopted as targets of the identification procedures. The variability of each parameter over the optimization runs and the different devices have been investigated through a statistical analysis, where the parameters mostly affecting the overall accuracy and dispersion have been identified, for each model. Finally, the Pareto front representation has been adopted aiming to identify the set of best performers both in terms of accuracy and robustness in reproducing the experimental behavior of devices.

It is observed that within the class of algebraic models, Law #1 is the best one to guarantee numerical stability in the reproduction of the experimental behavior over all the devices of the production series. On the contrary, Law #2 can be preferred for maximizing the accuracy of the model with a significant increase of the dispersion (30%) of the results among the devices. Law #3 represents a good compromise between the two previous configurations with a level of discrepancy with respect to the experimental input of 9% and a reliability level of about 22%.

On the other hand, Abe et al. model (i.e. law #5) is the best choice among differential models. As observed from the Pareto Front representation, it clearly dominates the other differential models (law #4 and #6). Additionally, it represents the best trade-off solution among all the investigated models able to simultaneously minimize errors in the accuracy of the reproduction of the experimental results and dispersion over all the devices and optimization runs.

Despite these results, it should be noted that the proposed procedure aims to provide valuable support for the case-by-case assessment of the best model according to the practitioner's objectives which would prioritize accuracy, ensure robustness in mass production, or strike an optimal balance between both. The selection process is facilitated by the proposed Pareto front representation, providing a clear framework for evaluating trade-offs between accuracy and robustness.

A limitation of this study can be found in its focus on unidirectional behavior for both the tested devices and the identified models. Typically, rubber isolators can perform in a bidirectional fashion and are tested in the horizontal plane following "circular" or "8-shape" trajectories. Despite this limitation, it is worth considering how in some cases (e.g., the Abe et al. law) the models analyzed allow for parameters' generalization. In other words, the parameters identified in the unidirectional operation can be reasonably extended to the bidirectional one.

Future Developments will be devoted to assess the goodness of the developed identification procedure when the influence of the variability production of HDRBs to the seismic response of real-world inspired buildings will be analyzed.

CRediT authorship contribution statement

Raffaele Cucuzza: Writing – review & editing, Writing – original draft, Validation, Software, Methodology, Investigation, Formal analysis, Data curation, Conceptualization. **Santiago Londoño:** Writing – original draft, Visualization, Validation, Software, Resources, Formal analysis, Data curation. **Marco Domaneschi:** Writing – review & editing, Supervision, Project administration, Methodology, Investigation, Formal analysis, Data curation, Conceptualization. **Rita Greco:** Writing – review & editing, Validation, Investigation, Conceptualization. **Giuseppe Carlo Marano:** Writing – review & editing, Supervision, Project administration, Methodology, Conceptualization.

Declaration of competing interest

The authors declare that they have no known competing financial interests or personal relationships that could have appeared to influence the work reported in this paper.

Acknowledgments

The research leading to these results has received funding from (i) the Project PNRR - MUR DM 118 - CUP E14D23001710006118/2023, (ii) the European Research Council under the Grant agreement ID: 101007595 of the project ADDOPTML, MSCA RISE 2020 Marie Skodowska Curie Research and Innovation Staff Exchange (RISE), and (iii) the Project Bando Prin 2022 - Decreto 749 Direttoriale n. 104 del 02-02-2022 - CUP E53C24002680006. SISMALAB in Crispiano (Taranto, Italy) is gratefully acknowledged for providing the test data.

Appendix

See Table A.5.

Table A.5
Optimal parameters for each law along the entire mass production

		Device 1		Device 2		Device 3		Device 4		Device 5	
		μ	σ	μ	σ	μ	σ	μ	σ	μ	σ
Law 1	**OF**	0.11	5.24E−03	0.14	6.88E−03	0.14	4.69E−03	0.13	3.85E−03	0.13	4.63E−03
	K_1	1.60	0.07	1.87	5.71E−02	1.79	6.71E−02	1.65	5.10E−02	1.69	7.88E−02
	K_2	0.40	0.01	0.45	9.88E−03	0.44	8.94E−03	0.43	1.03E−02	0.43	1.09E−02
	F_y	34.50	3.78	34.65	3.17	52.20	3.61	40.60	3.17	43.40	2.23

		Device 6		Device 7		Device 8		Device 9		Device 10	
		μ	σ	μ	σ	μ	σ	μ	σ	μ	σ
Law 1	**OF**	0.14	5.03E−03	0.14	4.54E−03	0.14	3.85E−03	0.15	4.00E−03	0.15	3.42E−03
	K_1	1.65	8.87E−02	1.65	6.86E−02	1.68	7.68E−02	1.67	5.87E−02	1.64	5.87E−02
	K_2	0.39	9.10E−03	0.42	1.02E−02	0.41	1.01E−02	0.40	9.12E−03	0.39	9.73E−03
	F_y	41.85	3.70	41.90	3.31	45.80	3.66	44.35	2.68	42.60	2.98

		Device 1		Device 2		Device 3		Device 4		Device 5	
		μ	σ	μ	σ	μ	σ	μ	σ	μ	σ
Law 2	**OF**	0.07	3.91E−03	0.07	2.29E−03	0.12	1.33E−03	0.06	2.42E−03	0.07	2.93E−03
	a_1	2.32E+05	6.72E+04	2.70E+05	7.47E+04	3.10E+05	4.22E+04	3.12E+05	6.92E+04	2.97E+05	5.06E+04
	a_2	2.97E+06	1.27E+06	3.41E+06	1.32E+06	4.55E+06	1.02E+06	4.73E+06	1.56E+06	4.59E+06	1.08E+06
	a_3	4.98E+06	2.14E+06	4.78E+06	1.85E+06	6.47E+06	1.78E+06	5.08E+06	1.50E+06	5.65E+06	1.81E+06
	a_4	2.85E+04	1.49E+04	4.17E+04	1.86E+04	4.67E+04	2.30E+04	3.87E+04	2.06E+04	4.21E+04	2.39E+04
	a_5	5.59E+03	1.72E+03	5.41E+03	2.72E+03	4.84E+03	2.19E+03	5.79E+03	1.16E+03	5.14E+03	1.71E+03
	a_6	1.06E+06	1.01E+05	1.25E+06	8.32E+04	1.80E+06	3.01E+05	1.10E+06	2.15E+05	1.26E+06	1.69E+05
	a_7	3.67	0.54	3.82	0.49	4.40	0.42	4.80	1.15	4.18	0.77
	a_8	11.99	1.36	11.93	0.85	16.06	1.90	14.95	1.98	15.10	1.86
	a_9	6.20E+04	1.33E+04	5.18E+04	3.32E+03	5.09E+04	3.61E+03	5.06E+04	2832.80	5.32E+04	4.36E+03
	a_{10}	5.60E+04	2.10E+04	6.33E+04	2.34E+04	6.71E+04	2.06E+04	7.98E+04	1.61E+04	7.65E+04	1.97E+04
	a_{11}	0.85	0.25	0.40	6.10E−02	0.36	6.57E−02	0.41	5.84E−02	0.43	8.16E−02

		Device 6		Device 7		Device 8		Device 9		Device 10	
		μ	σ	μ	σ	μ	σ	μ	σ	μ	σ
Law 2	**OF**	0.07	2.41E−03	0.07	2.39E−03	0.10	5.54E−04	0.08	1.93E−03	0.08	1.72E−03
	a_1	2.50E+05	5.40E+04	3.22E+05	3.38E+04	2.83E+05	4.42E+04	2.97E+05	4.98E+04	3.17E+05	3.10E+04
	a_2	4.53E+06	1.25E+06	4.40E+06	8.87E+05	4.72E+06	1.16E+06	4.36E+06	1.10E+06	3.73E+06	7.46E+05
	a_3	5.17E+06	1.74E+06	5.46E+06	2.16E+06	6.67E+06	1.31E+06	4.99E+06	1.89E+06	5.57E+06	1.84E+06
	a_4	4.02E+04	2.22E+04	5.05E+04	1.72E+04	2.56E+04	2.34E+04	3.80E+04	1.94E+04	4.38E+04	2.35E+04
	a_5	5.98E+03	2.07E+03	5.81E+03	1.83E+03	5.74E+03	1.89E+03	6.01E+03	2.35E+03	6.27E+03	2.28E+03
	a_6	1.25E+06	2.34E+05	1.25E+06	1.74E+05	1.46E+06	1.57E+05	1.18E+06	1.75E+05	1.15E+06	1.81E+05
	a_7	4.31	0.81	5.06	0.82	4.26	0.63	4.64	0.85	4.86	0.68
	a_8	14.99	2.05	16.24	1.23	16.34	1.33	14.91	1.67	14.98	1.56
	a_9	4.89E+04	3.17E+03	4.95E+04	2.83E+03	5.26E+04	2.23E+03	5.13E+04	3.11E+03	4.97E+04	3.11E+03
	a_{10}	7.86E+04	1.75E+04	7.72E+04	1.63E+04	6.87E+04	1.80E+04	8.69E+04	9.83E+03	8.07E+04	1.26E+04
	a_{11}	0.38	6.24E−02	0.39	5.13E−02	0.41	4.48E−02	0.38	5.32E−02	0.39	5.60E−02

		Device 1		Device 2		Device 3		Device 4		Device 5	
		μ	σ	μ	σ	μ	σ	μ	σ	μ	σ
Law 3	**OF**	0.09	3.83E−05	0.10	9.86E−05	0.10	1.75E−04	0.08	1.25E−04	0.08	1.01E−04
	K_{b+}	3.97E+05	7.69E+02	4.55E+05	1.86E+03	4.54E+05	1.86E+03	4.47E+05	1.83E+03	4.53E+05	1.60E+03
	K_{b-}	3.95E+05	5.59E+02	4.62E+05	1.47E+03	4.53E+05	2.82E+03	4.44E+05	3.39E+03	4.40E+05	1.97E+03
	F_{0+}	3.55E+04	0.00	4.35E+04	2.76E+02	5.10E+04	2.55E+02	4.26E+04	2.94E+02	4.44E+04	1.83E+02
	F_{0-}	3.60E+04	1.54E+02	4.33E+04	2.94E+02	3.87E+04	2.94E+02	4.26E+04	2.75E+02	4.21E+04	3.20E+02
	α_+	42.87	0.93	49.90	0.09	49.46	0.46	49.52	0.35	49.62	0.30
	α_-	38.08	0.53	49.75	0.20	49.70	0.23	49.64	0.35	49.72	0.20
	β_{1+}	0.24	0.17	0.37	0.22	0.38	0.21	0.31	0.23	0.37	0.18
	β_{1-}	−0.26	0.15	−0.35	0.15	−0.55	0.20	−0.53	0.09	−0.41	0.19
	β_{2+}	21.90	3.08	25.90	4.45	24.15	4.39	25.50	4.30	24.10	4.46
	β_{2-}	−20.70	2.83	−26.55	3.91	−41.15	3.42	−40.70	1.66	−33.55	3.90

(*continued on next page*)

Table A.5 (*continued*).

		Device 6		Device 7		Device 8		Device 9		Device 10	
		μ	σ	μ	σ	μ	σ	μ	σ	μ	σ
Law 3	**OF**	0.09	1.30E−04	0.08	2.60E−04	0.08	1.77E−04	0.09	2.02E−04	0.09	1.65E−04
	K_{b+}	4.04E+05	1.28E+03	4.39E+05	1.72E+03	4.33E+05	1.68E+03	4.39E+05	1.97E+03	4.35E+05	1.90E+03
	K_{b-}	3.89E+05	2.06E+03	4.27E+05	3.06E+03	4.18E+05	2.96E+03	3.82E+05	4.40E+03	3.80E+05	3.39E+03
	F_{0+}	4.17E+04	2.45E+02	4.31E+04	2.62E+02	4.87E+04	2.45E+02	4.39E+04	2.05E+02	4.15E+04	2.29E+02
	F_{0-}	4.36E+04	2.45E+02	4.22E+04	2.94E+02	3.79E+04	2.75E+02	4.65E+04	5.10E+02	4.63E+04	4.99E+02
	α_+	49.68	0.26	49.52	0.31	49.52	0.32	49.67	0.29	49.69	0.22
	α_-	49.60	0.39	49.60	0.40	49.60	0.37	49.54	0.33	49.74	0.28
	β_{1+}	0.40	0.21	0.36	0.18	0.39	0.21	0.30	0.17	0.36	0.23
	β_{1-}	−0.50	0.13	−0.50	0.18	−0.54	0.18	−0.70	0.13	−0.58	0.17
	β_{2+}	24.90	4.28	23.60	4.51	25.50	3.44	25.00	5.03	23.65	4.38
	β_{2-}	−36.25	2.67	−39.40	4.99	−34.55	6.05	−43.40	1.31	−42.10	1.97

		Device 1		Device 2		Device 3		Device 4		Device 5	
		μ	σ	μ	σ	μ	σ	μ	σ	μ	σ
Law 4	**OF**	0.09	2.65E−03	0.09	6.61E−04	0.12	4.03E−04	0.07	6.61E−04	0.08	7.25E−04
	α	0.20	0.02	0.14	1.69E−02	0.19	2.02E−02	0.12	2.08E−02	0.16	1.35E−02
	Ke	2.27	0.37	3.32	0.37	3.12	0.37	3.18	0.43	3.22	0.32
	A	1.10	0.07	1.10	0.12	1.60	0.23	1.10	0.22	1.40	0.12
	β	0.03	0.00	0.05	9.09E−03	0.05	7.83E−03	0.06	7.69E−03	0.05	5.25E−03
	n	1.00	0.02	1.05	3.43E−02	1.00	3.43E−02	1.00	2.22E−02	1.00	2.22E−02
	γ	0.03	0.01	0.03	3.35E−03	0.03	3.43E−03	0.03	3.66E−03	0.03	2.86E−03

		Device 6		Device 7		Device 8		Device 9		Device 10	
		μ	σ	μ	σ	μ	σ	μ	σ	μ	σ
Law 4	**OF**	0.08	7.46E−04	0.07	6.66E−04	0.11	6.39E−04	0.09	3.48E−04	0.09	5.96E−04
	α	0.11	2.39E−02	0.18	2.20E−02	0.13	1.36E−02	0.14	1.90E−02	0.13	1.66E−02
	Ke	3.15	0.51	3.02	0.42	3.14	0.29	3.24	0.41	3.27	0.42
	A	1.10	0.30	1.50	0.22	1.10	0.16	1.50	0.25	1.40	0.18
	β	0.06	7.50E−03	0.05	7.85E−03	0.05	6.93E−03	0.06	7.09E−03	0.06	6.26E−03
	n	1.00	2.35E−02	1.00	2.35E−02	1.00	2.05E−02	1.00	2.99E−02	1.05	2.55E−02
	γ	0.03	5.91E−03	0.03	4.01E−03	0.03	5.20E−03	0.03	3.02E−03	0.03	7.00E−03

		Device 1		Device 2		Device 3		Device 4		Device 5	
		μ	σ	μ	σ	μ	σ	μ	σ	μ	σ
Law 5	**OF**	0.08	2.00E−03	0.09	1.93E−03	0.12	7.62E−04	0.07	2.31E−03	0.07	2.11E−03
	K_1	6.84	0.83	6.83	1.01	6.99	1.11	7.14	1.17	7.45	1.02
	α	1.64	1.10	2.23	1.17	4.51	1.73	2.95	1.47	2.87	1.62
	β	0.03	0.01	0.03	1.37E−02	0.04	1.14E−02	0.03	8.65E−03	0.03	1.02E−02
	a	0.75	0.11	0.83	0.13	0.76	0.13	0.71	0.11	0.79	0.12
	b	7.05	1.02	7.29	1.19	7.47	0.92	7.29	0.95	7.14	1.30
	n	0.24	0.05	0.19	0.13	0.33	0.12	0.30	0.15	0.34	0.12
	Y_0	51.15	6.98	60.75	10.26	50.10	10.26	49.50	9.97	47.05	7.63
	X_h	117.10	20.39	107.80	16.16	117.40	19.50	114.70	20.80	113.70	17.12
	p	1.65	0.24	1.69	0.20	1.80	0.13	1.68	0.22	1.74	0.20
	X_0	4.87	0.57	3.03	0.77	2.55	0.28	2.80	0.58	2.51	0.30
	X_s	25.40	5.80	30.50	9.17	38.80	10.13	41.75	6.17	41.65	7.82
	K_2	0.14	0.05	0.19	7.41E−02	0.19	7.10E−02	0.22	6.83E−02	0.19	5.67E−02
	r	0.08	0.04	0.06	3.73E−02	0.10	6.79E−02	0.12	5.25E−02	0.06	3.59E−02

		Device 6		Device 7		Device 8		Device 9		Device 10	
		μ	σ	μ	σ	μ	σ	μ	σ	μ	σ
Law 5	**OF**	0.07	2.02E−03	0.07	2.40E−03	0.10	1.00E−03	0.09	1.66E−03	0.09	1.17E−03
	K_1	7.22	1.13	7.12	1.19	6.74	1.08	7.32	1.13	7.37	1.25
	α	3.14	1.07	2.45	0.88	4.59	1.65	3.03	1.56	2.47	1.53
	β	0.03	8.93E−03	0.03	1.30E−02	0.03	1.42E−02	0.03	9.39E−03	0.03	9.47E−03
	a	0.76	0.12	0.75	0.15	0.84	0.09	0.72	0.16	0.75	0.12
	b	7.78	1.20	7.26	1.32	7.10	1.28	7.47	1.25	7.81	1.18
	n	0.31	0.11	0.34	0.14	0.28	0.09	0.31	0.13	0.21	0.11
	Y_0	47.50	9.80	47.45	9.18	48.60	6.90	47.70	7.79	53.05	10.71
	X_h	117.60	17.24	110.30	18.53	117.40	17.24	124.60	20.65	109.90	18.54
	p	1.73	0.18	1.73	0.16	1.71	0.19	1.64	0.40	1.70	0.12
	X_0	2.43	0.24	2.45	0.28	2.47	0.28	2.43	0.31	2.64	0.41
	X_s	41.15	10.28	39.15	10.35	40.10	7.58	40.05	8.20	37.00	10.96
	K_2	0.17	6.52E−02	0.20	7.27E−02	0.18	9.21E−02	0.15	5.89E−02	0.17	6.46E−02
	r	0.09	4.08E−02	0.11	4.01E−02	0.06	3.86E−02	0.09	3.17E−02	0.10	5.09E−02

(*continued on next page*)

Table A.5 (*continued*).

		Device 1		Device 2		Device 3		Device 4		Device 5	
		μ	σ	μ	σ	μ	σ	μ	σ	μ	σ
	OF	0.12	2.40E−03	0.14	8.72E−04	0.14	3.61E−03	0.10	5.37E−03	0.10	2.16E−03
	a_1	4.29E+03	1.43E+02	5.05E+03	97.20	4.90E+03	152.09	4.61E+03	84.72	4.73E+03	123.97
	a_2	−1.29	0.58	−1.42	0.57	−0.76	0.38	−0.73	0.29	−0.97	0.45
	a_3	0.01	0.00	0.01	8.45E−04	0.01	5.69E−04	0.01	2.87E−04	0.01	7.33E−04
	a_4	60.04	12.47	56.10	12.58	55.80	13.33	54.56	14.90	50.95	14.77
Law 6	a_5	0.45	0.19	0.43	0.19	0.46	0.23	0.50	0.24	0.44	0.21
	a_6	5.27E+04	8.05E+03	5.74E+04	9.40E+02	6.33E+04	7.98E+03	6.12E+04	1.17E+04	5.79E+04	3.04E+03
	a_7	5.07	1.44	6.66	1.15	5.60	1.56	6.54	1.23	6.58	0.87
	a_8	66.95	17.48	50.35	0.67	56.50	12.28	57.90	19.00	51.80	4.41
	a_9	−3.07E−06	1.20E−06	−2.68E−06	9.64E−07	−2.16E−06	1.12E−06	−3.00E−06	1.10E−06	−2.24E−06	7.65E−07
	a_{10}	−1.05E−07	1.23E−07	−1.65E−07	1.04E−07	−1.20E−06	4.43E−06	−2.12E−06	5.27E−06	−1.47E−06	3.86E−06

		Device 6		Device 7		Device 8		Device 9		Device 10	
		μ	σ	μ	σ	μ	σ	μ	σ	μ	σ
	OF	0.11	1.89E−03	0.10	1.84E−03	0.12	3.05E−03	0.12	1.69E−03	0.12	1.35E−03
	a_1	4.21E+03	92.62	4.45E+03	66.69	4.69E+03	95.80	4.51E+03	74.16	4.47E+03	105.48
	a_2	−1.06	0.29	−0.68	0.25	−1.31	0.46	−1.06	0.29	−1.14	0.46
	a_3	0.01	4.09E−04	0.01	3.20E−04	0.01	7.43E−04	0.01	4.18E−04	0.01	5.20E−04
	a_4	50.18	18.96	50.22	16.84	55.54	14.54	54.71	17.82	53.53	10.59
Law 6	a_5	0.46	0.25	0.47	0.20	0.44	0.22	0.48	0.25	0.47	0.19
	a_6	5.65E+04	1.28E+03	5.69E+04	1.35E+03	6.09E+04	4.77E+03	5.83E+04	1.13E+03	5.62E+04	875.09
	a_7	5.98	1.55	6.78	0.77	5.98	1.29	6.29	1.01	6.61	1.12
	a_8	51.05	1.50	51.00	1.89	54.55	7.08	50.85	1.63	50.80	1.32
	a_9	−2.07E−06	9.20E−07	−2.14E−06	1.15E−06	−2.56E−06	1.10E−06	−2.39E−06	1.21E−06	−2.71E−06	1.03E−06
	a_{10}	−2.05E−07	1.93E−07	−2.97E−06	5.38E−06	−2.03E−06	6.08E−06	−5.39E−06	8.41E−06	−2.66E−06	5.49E−06

References

[1] Kelly JM. Earthquake-resistant design with rubber, vol. 7, Springer; 1993.

[2] Nakashima M, Pan P, Zamfirescu D, Weitzmann R. Post-kobe approach for design and construction of base-isolated buildngs. J Jpn Assoc Earthq Eng 2004;4(3):259–64.

[3] Fujita T, Fujita S, Tazaki S, Yoshizawa T, Suzuki S. Research, development and implementation of rubber bearings for seismic isolation. JSME Int J Ser 3, Vib Control Eng Eng Ind 1990;33(3):394–403.

[4] Warn GP, Ryan KL. A review of seismic isolation for buildings: historical development and research needs. Buildings 2012;2(3):300–25.

[5] Clemente P, Martelli A. Seismically isolated buildings in Italy: State-of-the-art review and applications. Soil Dyn Earthq Eng 2019;119:471–87. http://dx.doi.org/10.1016/j.soildyn.2017.12.029.

[6] Ismail M, Rodellar J, Carusone G, Domaneschi M, Martinelli L. Characterization, modeling and assessment of Roll-N-Cage isolator using the cable-stayed bridge benchmark. Acta Mech 2013;224(3):525–47. http://dx.doi.org/10.1007/s00707-012-0771-4.

[7] De Mari G, Domaneschi M, Ismail M, Martinelli L, Rodellar J. Reduced-order coupled bidirectional modeling of the Roll-N-Cage isolator with application to the updated bridge benchmark. Acta Mech 2015;226(10):3533–53. http://dx.doi.org/10.1007/s00707-015-1394-3.

[8] De Luca A, Guidi LG. State of art in the worldwide evolution of base isolation design. Soil Dyn Earthq Eng 2019;125:105722.

[9] Cimellaro G, Domaneschi M, Warn G. Three-dimensional base isolation using vertical negative stiffness devices. J Earthq Eng 2020;24(12):2004–32. http://dx.doi.org/10.1080/13632469.2018.1493004.

[10] Architectural Institute of Japan. Design recommendations for seismically isolated buildings. Architectural Institute of Japan Tokyo, Japan; 2016.

[11] Tubaldi E, Mitoulis SA, Ahmadi H. Comparison of different models for high damping rubber bearings in seismically isolated bridges. Soil Dyn Earthq Eng 2018;104:329–45.

[12] Van Engelen NC. Fiber-reinforced elastomeric isolators: A review. Soil Dyn Earthq Eng 2019;125:105621.

[13] Miranda S, Miranda E, de la Llera JC. A simplified and versatile element model for elastomeric seismic isolation bearings. Earthq Spectra 2022;38(1):331–57.

[14] Deringöl AH, Güneyisi EM. Effect of using high damping rubber bearings for seismic isolation of the buildings. Int J Steel Struct 2021;21(5):1698–722.

[15] Marano GC. Probabilistic seismic response and reliability assessment of isolated bridges. Earthq Eng Eng Vib 2005;4(1):95–106.

[16] Marano GC, Sgobba S. Stochastic energy analysis of seismic isolated bridges. Soil Dyn Earthq Eng 2007;27(8):759–73.

[17] Gharehbaghi K. Advancements in concrete technology in Australia: Geo-polymer concrete. Int J Constr Environ 2015;7(1).

[18] Mazza F. Effects of the long-term behaviour of isolation devices on the seismic response of base-isolated buildings. Struct Control Heal Monit 2019;26(4):e2331.

[19] Gu Z, Lei Y, Qian W, Xiang Z, Hao F, Wang Y. An experimental study on the mechanical properties of a high damping rubber bearing with low shape factor. Appl Sci 2021;11(21):10059.

[20] Kumar M, Whittaker AS, Constantinou MC. An advanced numerical model of elastomeric seismic isolation bearings. Earthq Eng Struct Dyn 2014;43(13):1955–74.

[21] Domaneschi M, Martinelli L, Cattivelli C. Phenomenological model of rubber bearings with variable axial loading. Front Built Environ 2018;4:49.

[22] Pelliciari M, Marano GC, Cuoghi T, Briseghella B, Lavorato D, Tarantino AM. Parameter identification of degrading and pinched hysteretic systems using a modified Bouc–Wen model. Struct Infrastruct Eng 2018;14(12):1573–85.

[23] Eem S, Hahm D. Large strain nonlinear model of lead rubber bearings for beyond design basis earthquakes. Nucl Eng Technol 2019;51(2):600–6.

[24] Tsai C, Chiang T-C, Chen B-J, Lin S-B. An advanced analytical model for high damping rubber bearings. Earthq Eng Struct Dyn 2003;32(9):1373–87.

[25] Capuano R, Fraddosio A, Piccioni MD. Phenomenological rate-independent uniaxial hysteretic models: A mini-review. Front Built Environ 2022;8:1048533.

[26] Sansour C, Karsaj I, Soric J. On free energy-based formulations for kinematic hardening and the decomposition F=fpfe. Int J Solids Struct 2006;43(25–26):7534–52.

[27] Ramberg W, Osgood WR. Description of stress-strain curves by three parameters. Tech. rep. 1943.

[28] Menegotto M. Method of analysis for cyclically loaded RC plane frames including changes in geometry and non-elastic behavior of elements under combined normal force and bending. In: Proc. of IABSE symposium on resistance and ultimate deformability of structures acted on by well defined repeated loads, 1973. 1973.

[29] Masing G. Eigenspannungen und verfestigung beim messing. In: Proceedings, second international congress of applied mechanics. 1926, p. 332–5.

[30] Riegger H, Masing G, Mauksch W. Über das Verhalten von kalt gerecktem Messing bei Zug-und Stauchbelastung. Wiss Veröffentlichungen Aus Dem Siemens-Konzern 1926;142–55.

[31] Markou AA, Manolis GD. Mechanical formulations for bilinear and trilinear hysteretic models used in base isolators. Bull Earthq Eng 2016;14:3591–611.

[32] Jankowski R, Wilde K, Fujino Y. Reduction of pounding effects in elevated bridges during earthquakes. Earthq Eng Struct Dyn 2000;29(2):195–212.

[33] Yamamoto S, Kikuchi M, Ueda M, Aiken ID. A mechanical model for elastomeric seismic isolation bearings including the influence of axial load. Earthq Eng Struct Dyn 2009;38(2):157–80.

[34] Ozdemir H. Nonlinear transient dynamic analysis of yielding structures. University of California, Berkeley; 1976.

[35] Graesser E, Cozzarelli F. Shape-memory alloys as new materials for aseismic isolation. J Eng Mech 1991;117(11):2590–608.

[36] Sheikh H, Van Engelen NC, Ruparathna R. A review of base isolation systems with adaptive characteristics. In: Structures, vol. 38, Elsevier; 2022, p. 1542–55.

[37] Capuano R, Fraddosio A, Piccioni M. Phenomenological rate-independent uniaxial hysteretic models: A mini-review. Front Built Environ 2022;8:1048533. http://dx.doi.org/10.3389/fbuil.2022.1048533.

[38] Olivo J, Cucuzza R, Bertagnoli G, Domaneschi M. Optimal design of steel exoskeleton for the retrofitting of RC buildings via genetic algorithm. Comput Struct 2024;299:107396.
[39] Cucuzza R, Aloisio A, Domaneschi M, Nascimbene R. Multimodal seismic assessment of infrastructures retrofitted with exoskeletons: insights from the Foggia Airport case study. Bull Earthq Eng 2024;1–29.
[40] Quaranta G, Marano G, Greco R, Monti G. Parametric identification of seismic isolators using differential evolution and particle swarm optimization. Appl Soft Comput J 2014;22:458–64, URL https://www.scopus.com/inward/record.uri?eid=2-s2.0-84903738365&doi=10.1016%2fj.asoc.2014.04.039&partnerID=40&md5=f3dca21b3e938909a12e8da41f1da5d2.
[41] Marano G, Quaranta G, Monti G. Modified genetic algorithm for the dynamic identification of structural systems using incomplete measurements. Computer-Aided Civ Infrastruct Eng 2011;26(2):92–110, URL https://www.scopus.com/inward/record.uri?eid=2-s2.0-78651435257&doi=10.1111%2fj.1467-8667.2010.00659.x&partnerID=40&md5=655d045ec2a46f7aad438178878d58c6.
[42] Marano G, Quaranta G, Avakian J, Palmeri A. Identification of passive devices for vibration control by evolutionary algorithms. 2013, p. 373–87, URL https://www.scopus.com/inward/record.uri?eid=2-s2.0-84882603167&doi=10.1016%2fB978-0-12-398364-0.00015-2&partnerID=40&md5=0be21dc5e85f48e7fb8375249dfc60aa,
[43] Pauletta M, Cortesia A, Pitacco I, Russo G. A new bi-linear constitutive shear relationship for unbonded fiber-reinforced elastomeric isolators (U-FREIs). Compos Struct 2017;168:725–38.
[44] Liu T, Zordan T, Briseghella B, Zhang Q. An improved equivalent linear model of seismic isolation system with bilinear behavior. Eng Struct 2014;61:113–26.
[45] Jankowski R. Non-linear model of high damping rubber bearing. 2004.
[46] Jankowski R. Nonlinear rate dependent model of high damping rubber bearing. Bull Earthq Eng 2003;1:397–403.
[47] Vaiana N, Sessa S, Rosati L. A generalized class of uniaxial rate-independent models for simulating asymmetric mechanical hysteresis phenomena. Mech Syst Signal Process 2021;146:106984.
[48] Kikuchi M, Aiken ID. An analytical hysteresis model for elastomeric seismic isolation bearings. Earthq Eng Struct Dyn 1997;26(2):215–31.
[49] Pellecchia D, Lo Feudo S, Vaiana N, Dion J-L, Rosati L. A procedure to model and design elastomeric-based isolation systems for the seismic protection of rocking art objects. Computer- Aided Civ Infrastruct Eng 2022;37(10):1298–315.
[50] Vaiana N, Sessa S, Marmo F, Rosati L. Nonlinear dynamic analysis of hysteretic mechanical systems by combining a novel rate-independent model and an explicit time integration method. Nonlinear Dynam 2019;98:2879–901.
[51] Bouc R. Forced vibrations of mechanical systems with hysteresis. In: Proc. of the fourth conference on nonlinear oscillations. 1967.
[52] Domaneschi M. Simulation of controlled hysteresis by the semi-active Bouc-Wen model. Comput Struct 2012;106–107:245–57. http://dx.doi.org/10.1016/j.compstruc.2012.05.008, cited By 43.
[53] Ismail M, Ikhouane F, Rodellar J. The hysteresis Bouc-Wen model, a survey. Arch Comput Methods Eng 2009;16(2):161–88. http://dx.doi.org/10.1007/s11831-009-9031-8, cited By 557.
[54] Abe M, Yoshida J, Fujino Y. Multiaxial behaviors of laminated rubber bearings and their modeling. I: Experimental study. J Struct Eng 2004;130(8):1119–32.
[55] Yoshida J, Abe M, Fujino Y. Constitutive model of high-damping rubber materials. J Eng Mech 2004;130(2):129–41.
[56] Perotti F, Domaneschi M, De Grandis S. The numerical computation of seismic fragility of base-isolated nuclear power plants buildings. Nucl Eng Des 2013;262:189–200.
[57] Hwang J, Wu J, Pan T-C, Yang G. A mathematical hysteretic model for elastomeric isolation bearings. Earthq Eng Struct Dyn 2002;31(4):771–89.
[58] Hwang J, Ku S. Analytical modeling of high damping rubber bearings. J Struct Eng 1997;123(8):1029–36.
[59] Hwang J, Wang J. Seismic response prediction of HDR bearings using fractional derivative Maxwell model. Eng Struct 1998;20(9):849–56.
[60] Pan T, Yang G. Nonlinear analysis of base-isolated MDOF structures. In: Proceedings of the 11th world conference on earthquake engineering, paper, no. 1534. 1996, p. 1–8.
[61] UNI EN 15129-8.2.1.2.2: Anti-seismic devices – Testing requirements. UNI (Ente Nazionale Italiano di Unificazione); 2012, Italian Standard.
[62] Cucuzza R, Domaneschi M, Greco R, Marano GC. Numerical models comparison for fluid-viscous dampers: Performance investigations through genetic algorithm. Comput Struct 2023;288:107122. http://dx.doi.org/10.1016/j.compstruc.2023.107122.
[63] The MathWorks, Inc. MATLAB release R2023b. Natick, Massachusetts, United States; 2023, Available at: https://www.mathworks.com.
[64] Rosso MM, Cucuzza R, Aloisio A, Marano GC. Enhanced multi-strategy particle swarm optimization for constrained problems with an evolutionary-strategies-based unfeasible local search operator. Appl Sci 2022;12(5):2285.
[65] Mitchell M. Genetic algorithms: An overview. Complexity 1995;1(1):31–9.
[66] Beaslev D, Bull DR, Martin RR. An overview of genetic algorithms: Part 2, research topics. Univ Comput 1993;15(4).
[67] Tomassini M. A survey of genetic algorithms. Annu Rev Comput Phys III 1995;87–118.